



# Black holes surrounded by PFDM in Kalb-Ramond gravity: from thermodynamics to QPO tests

Shokhzod Jumaniyozov<sup>1,2,a</sup> , Sardor Murodov<sup>1,3,b</sup> , Javlon Rayimbaev<sup>4,5,6,c</sup> , Inomjon Ibragimov<sup>7,d</sup> ,  
Bekzod Madaminov<sup>8,e</sup> , Sharofiddin Urinbaev<sup>9,f</sup> , Ahmadjon Abdujabbarov<sup>10,11,g</sup> 

- <sup>1</sup> New Uzbekistan University, Movarounnahr Street 1, 100000 Tashkent, Uzbekistan  
<sup>2</sup> Tashkent International University of Education, Imom Bukhoriy 6, 100207 Tashkent, Uzbekistan  
<sup>3</sup> Institute of Fundamental and Applied Research, Kori Niyoziy 39, 100000 Tashkent, Uzbekistan  
<sup>4</sup> National University of Uzbekistan, 100174 Tashkent, Uzbekistan  
<sup>5</sup> University of Tashkent for Applied Sciences, Str. Gavhar 1, 100149 Tashkent, Uzbekistan  
<sup>6</sup> Urgench State University, Kh. Alimjan Str. 14, 221100 Urgench, Uzbekistan  
<sup>7</sup> Kimyo International University in Tashkent, Shota Rustaveli street 156, 100121 Tashkent, Uzbekistan  
<sup>8</sup> Mamun University, Bolkhovuz Street 2, 220900 Khiva, Uzbekistan  
<sup>9</sup> National Research University TIAME, Kori Niyoziy 39, 100000 Tashkent, Uzbekistan  
<sup>10</sup> School of Physics, Harbin Institute of Technology, 150001 Harbin, People's Republic of China  
<sup>11</sup> Tashkent State Technical University, 100095 Tashkent, Uzbekistan

Received: 16 April 2025 / Accepted: 14 July 2025  
© The Author(s) 2025

**Abstract** Studying black holes in alternative gravitational frameworks is crucial for understanding the interplay between dark matter and modified gravity. This work examines black holes immersed in perfect fluid dark matter (PFDM) within the Kalb–Ramond (KR) gravity framework. The KR field, a rank-2 antisymmetric tensor, introduces additional degrees of freedom that alter spacetime geometry and affect particle dynamics. We derive the metric for a black hole embedded in PFDM and analyze the circular motion of test particles. By investigating the effective potential, energy, and angular momentum, we determine conditions for stable circular orbits and explore the impact of KR field parameters and PFDM properties. Beyond kinematics, we study quasi-periodic oscillations (QPOs) commonly observed in the X-ray spectra of black hole accretion disks. We link QPO frequencies to orbital properties in our model, proposing an observational test to distinguish KR gravity with PFDM from general relativity. Additionally, we explore the thermodynamic aspects of these black holes, calculating temperature,

entropy, and heat capacity to assess the impact of the KR field and PFDM on stability and phase transitions. Radiation properties are also investigated, including modifications to radiation due to the influence of the PFDM and the KR field on the event horizon. Our results reveal that KR gravity and PFDM generate distinctive signatures in particle dynamics, QPO patterns, thermodynamics, and radiation, offering potential observational tests to differentiate these models from standard general relativity (GR).

## 1 Introduction

The study of black hole (BH) dynamics is a cornerstone of modern theoretical and astrophysical research that offers profound insights into the interplay between gravity, quantum mechanics, and astrophysical phenomena. In particular, exploring the behavior of test particles and their associated quasiperiodic oscillations (QPOs) around BHs is a crucial avenue to understanding the underlying physics of strong gravitational fields [1, 2].

The Kalb–Ramond gravity framework, which introduces an antisymmetric tensor field in gravitational theory, has gained traction as a promising modification of General Relativity (GR). This framework extends our understanding of fundamental forces and provides testable predictions in extreme environments such as black hole spacetimes [3–5].

<sup>a</sup> e-mail: [sh.jumaniyozov@newuu.uz](mailto:sh.jumaniyozov@newuu.uz)

<sup>b</sup> e-mail: [mursardor@ifar.uz](mailto:mursardor@ifar.uz)

<sup>c</sup> e-mail: [javlon@astrin.uz](mailto:javlon@astrin.uz) (corresponding author)

<sup>d</sup> e-mail: [i.ibragimov@kiut.uz](mailto:i.ibragimov@kiut.uz)

<sup>e</sup> e-mail: [madaminov\\_bekzod@mamunedu.uz](mailto:madaminov_bekzod@mamunedu.uz)

<sup>f</sup> e-mail: [sharofiddinurinbaev@gmail.com](mailto:sharofiddinurinbaev@gmail.com)

<sup>g</sup> e-mail: [ahmadjon@astrin.uz](mailto:ahmadjon@astrin.uz)

Furthermore, when BHs are surrounded by exotic forms of matter, such as perfect fluid dark matter or quintessence, their dynamics significantly differ from predictions based solely on vacuum solutions. The presence of a dark matter medium can influence particle trajectories, accretion disk structures, and even the QPO frequencies, making it a compelling area of investigation [6, 7]. The phenomenon of QPOs, observed in the X-ray emissions of accreting BH systems, is a valuable diagnostic tool for probing the spacetime geometry and the properties of compact objects. QPOs have been successfully used to constrain the mass and spin of BHs and to test alternative theories of gravity [8–10]. In this context, combining KR gravity and the perfect fluid dark matter model offers a novel platform for studying the modifications introduced to the BH environment and the corresponding observational signatures.

In this work, we aim to investigate the dynamics of test particles around BHs in KR gravity surrounded by PFDM. We focus on understanding how the antisymmetric tensor field and the dark matter medium alter the trajectories of particles and the characteristics of QPOs [7, 11–13]. By analyzing these effects, we hope to shed light on the potential observational imprints that could help distinguish between different gravitational models and the nature of dark matter. The structure of this manuscript is as follows: In Sect. 2, we will explore the spacetime characteristics around BHs in KR gravity with surrounding PFDM. Section 3, we conduct a detailed analysis of the thermodynamic parameters of the black hole under investigation, exploring its key properties and their physical implications. Section 4 focuses on analyzing the circular motion of neutral test particles. In Sect. 5, we research the radiation properties of the accretion disk around a BH. In Sect. 6, we will investigate quasi-periodic oscillations and different models of QPOs through the framework of fundamental frequencies. Lastly, in Sect. 8, we will summarize our findings and present concluding remarks. We adopt the spacetime metric signature  $(-, +, +, +)$  and work in the geometrized unit system where  $G = c = 1$ . Latin indices range from 1 to 3, while Greek indices vary from 0 to 3.

## 2 The spacetime properties

The action for a gravitational field in KR gravity, which includes contributions from the KR field [3], the BH's gravitational field, and the PFDM surrounding it, is generally written as:

$$S = S_{GR} + S_{KR} + S_{PFDM} \quad (1)$$

The standard Einstein–Hilbert action governs the spacetime geometry [14], given by:

$$S_{GR} = \frac{1}{16\pi G} \int \sqrt{-g} R d^4x \quad (2)$$

where  $R$ , the Ricci scalar curvature, describes the spacetime geometry.  $g = \det(g_{\mu\nu})$  is determinant of the spacetime metric tensor  $g_{\mu\nu}$ .  $G$  is the Newtonian gravitational constant. We have set  $8\pi G = 1$  for convenience.

The KR field is a rank-two antisymmetric tensor field  $B_{\mu\nu}$ . To produce a nonzero vacuum expectation value (VEV) for the KR field, denoted as  $\langle B_{\mu\nu} \rangle = b_{\mu\nu}$ , we adopt a potential of the general form  $V = V(B^{\mu\nu} B_{\mu\nu} \pm b^2)$ , with the  $\pm$  sign chosen to ensure  $b^2$  is a positive constant. This leads to the VEV being governed by the constant norm condition  $b^{\mu\nu} b_{\mu\nu} = \mp b^2$ . During vacuum condensation, the gauge symmetry  $B_{\mu\nu} \rightarrow B_{\mu\nu} + \partial_{[\mu} \Gamma_{\nu]}$  of the Kalb–Ramond field is spontaneously violated, resulting in a symmetry-breaking VEV background that disrupts particle local Lorentz invariance. Additionally, the term  $\xi_3 B^{\mu\nu} B_{\mu\nu} R$  in the action (1) becomes  $\mp \xi_3 b^2 R$  in the vacuum, which can be incorporated into the Einstein–Hilbert terms via a redefinition of variables.

Decomposing the KR field, it is practical to express the antisymmetric tensor  $B_{\mu\nu}$  as  $B_{\mu\nu} = E_{[\mu} v_{\nu]} + \epsilon_{\mu\nu\alpha\beta} v^\alpha \tilde{B}^\beta$ , where  $v^\alpha$  is a timelike 4-vector. The pseudofields  $\tilde{E}_\mu$  and  $\tilde{B}_\mu$  are spacelike, satisfying  $\tilde{E}_\mu v^\mu = \tilde{B}_\mu v^\mu = 0$ . Similar to Maxwell electrodynamics, these can be regarded as pseudo-electric and pseudomagnetic fields, respectively. By assuming that only  $b_{rt} = -b_{tr} = \tilde{E}(r)$  are nonzero in the VEV, or equivalently,  $\mathbf{b}_2 = -\tilde{E}(r) dt \wedge dr$  in differential form notation, the vacuum field takes on a pseudoelectric configuration. This arrangement naturally causes the KR field strength to vanish, i.e.,  $H_{\lambda\mu\nu} = 0$ .

KR dynamics are governed by a field strength tensor  $H_{\mu\nu\rho}$  is:

$$H_{\mu\nu\rho} = \partial_\mu B_{\nu\rho} + \partial_\nu B_{\rho\mu} + \partial_\rho B_{\mu\nu} = \partial_{[\mu} B_{\nu\rho]} \quad (3)$$

The corresponding action for the KR field [3] is:

$$S_{KR} = -\frac{1}{2} \int \sqrt{-g} \left[ \frac{1}{6} H_{\mu\nu\rho} H^{\mu\nu\rho} + V(B^{\mu\nu} B_{\mu\nu} \pm b^2) - \xi_2 B^{\rho\mu} B_\mu^\nu R_{\rho\nu} - \xi_3 B^{\mu\nu} B_{\mu\nu} R \right] d^4x \quad (4)$$

where  $\xi_{2,3}$  are the non-minimal coupling constants between gravity and the KR field.  $H_{\mu\nu\rho}$  is the kinetic term for the KR field.

The action for the PFDM is modeled as a perfect fluid with the energy-momentum tensor  $T_{\mu\nu}^{\text{PFDM}} = (\rho + p)u_\mu u_\nu + p g_{\mu\nu}$ , where,  $\rho$  is an energy density, and pressure  $p$ . The energy-momentum tensor  $T_\nu^\mu = \text{diag}(-\rho, p_r, p_\theta, p_\phi)$  with

$$-\rho = p_r = \frac{\lambda}{8\pi r^3} \quad \text{and} \quad p_\theta = p_\phi = -\frac{\lambda}{16\pi r^3}. \quad (5)$$

To obtain the field equations, we vary the action concerning the metric tensor  $g_{\mu\nu}$ , the KR field  $B_{\mu\nu}$ , and, if applicable, other dynamical fields. Here, we focus on the gravitational field equations resulting from the variation for  $g_{\mu\nu}$ . The variation of the action  $S$  with respect to  $g_{\mu\nu}$  yields:

$$R_{\mu\nu} - \frac{1}{2}g_{\mu\nu}R = T_{\mu\nu}^{\text{KR}} + T_{\mu\nu}^{\text{PFDM}}, \quad (6)$$

where  $R_{\mu\nu}$  the Ricci tensor and  $T_{\mu\nu}^{\text{KR}}$  is the energy-momentum tensor of the KR field, and it has the form,

$$\begin{aligned} T_{\mu\nu}^{\text{KR}} = & \frac{1}{2}H_{\mu\rho\lambda}H_{\nu}{}^{\rho\lambda} - \frac{1}{2}g_{\mu\nu}H^{\rho\lambda\sigma}H_{\rho\lambda\sigma} + 2V'(Y)B_{\mu\rho}B^{\rho}{}_{\nu} \\ & - g_{\mu\nu}V(Y) + \xi_2 \left[ \frac{1}{2}g_{\mu\nu}B^{\rho\sigma}B^{\lambda}{}_{\sigma}R_{\rho\lambda} - B^{\rho}{}_{\mu}B^{\lambda}{}_{\nu}R_{\rho\lambda} \right. \\ & - B^{\rho\lambda}B_{\nu\lambda}R_{\mu\rho} - B^{\rho\lambda}B_{\mu\lambda}R_{\nu\rho} + \frac{1}{2}\nabla_{\rho}\nabla_{\mu}(B^{\rho\lambda}B_{\nu\lambda}) \\ & + \frac{1}{2}\nabla_{\rho}\nabla_{\nu}(B^{\rho\lambda}B_{\mu\lambda}) - \frac{1}{2}\nabla^{\rho}\nabla_{\rho}(B_{\mu}{}^{\lambda}B_{\nu\lambda}) \\ & \left. - \frac{1}{2}g_{\mu\nu}\nabla_{\rho}\nabla_{\lambda}(B^{\rho\sigma}B^{\lambda}{}_{\sigma}) \right] \end{aligned} \quad (7)$$

where parentheses denote symmetrization over indices, and  $\nabla^{\lambda}$  is the covariant derivative. This tensor includes contributions from the kinetic term of the KR field ( $H_{\mu\nu\rho}$ ), the potential  $V$ , and the non-minimal couplings  $\xi_2$  and  $\xi_3$  between the KR field and curvature tensors.  $Y = 2b_{\mu\rho}b_{\nu}{}^{\rho} + b^2g_{\mu\nu}$

Exploring a static and spherically symmetric spacetime within the nonzero VEV background of the KR field, we propose the metric ansatz

$$ds^2 = -A(r)dt^2 + B(r)dr^2 + r^2d\theta^2 + r^2\sin^2\theta d\phi^2. \quad (8)$$

Accordingly, the pseudoelectric field  $\tilde{E}(r)$  can be expressed as  $\tilde{E}(r) = |b|\sqrt{A(r)B(r)}/2$ , ensuring that the constant norm condition  $b^{\mu\nu}b_{\mu\nu} = -b^2$  is fulfilled.

The following differential equations are obtained using the field equation (6) under the ansatz  $A(r) = 1/B(r) = f(r)$ :

$$f''(r) + \frac{2}{r}f'(r) + \frac{\lambda}{2r^3} = 0, \quad (9)$$

$$f''(r) + \frac{1+l}{lr}f'(r) - \frac{1}{lr^2} + \frac{1-l}{lr^2}f(r) = 0. \quad (10)$$

where  $l \equiv \xi_2 b^2/2$  [3]. Using Eqs. (9) and (10), one can easily get,

$$rf'(r) + f(r) - \frac{1}{1-l} - \frac{\lambda}{r} = 0 \quad (11)$$

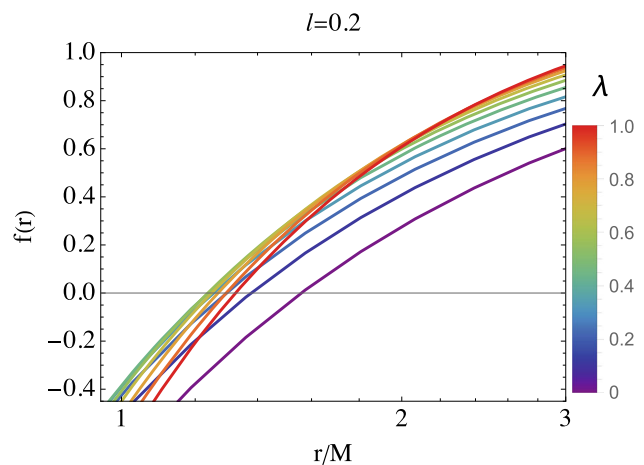


**Fig. 1** The radial dependence of the metric function for a BH in KR gravity surrounded by PFDM is shown for different parameter values  $\lambda$ , with  $l = 0.2$  fixed

which has the solution

$$f(r) = \frac{1}{1-l} + \frac{\lambda}{r} \ln r + \frac{c_1}{r} \quad (12)$$

where the constant have to be  $c_1 = -2M - \lambda \ln |\lambda|$ , to satisfy the solution KR and GR limits.

Thus the metric function  $f(r)$  is defined as:

$$f(r) = \frac{1}{1-l} - \frac{2M}{r} + \frac{\lambda}{r} \ln \frac{r}{|\lambda|}. \quad (13)$$

The logarithmic term in the lapse function is a unique signature of the surrounding dark matter’s effect, while the  $\frac{1}{1-l}$  factor indicates the KR corrections. This metric generalizes the Schwarzschild solution and exhibits deviations near the event horizon of the BH.

In Fig. 1, we present the radial dependence of the lapse function  $f(r)$  for the spacetime surrounding the BH in KR gravity with PFDM for  $l = 0.2$ . The PFDM parameter influences the behavior of the metric function. From the figure, it is evident that an increase in the parameter  $\lambda$  leads to a rise in the value of the metric function.

### 2.1 Event horizon: the ultimate boundary of BHs

The event horizon represents the ultimate boundary beyond which nothing, not even light, can escape. It is determined by setting the lapse function to zero, defining the fundamental characteristic of BHs. The event horizon can be expressed

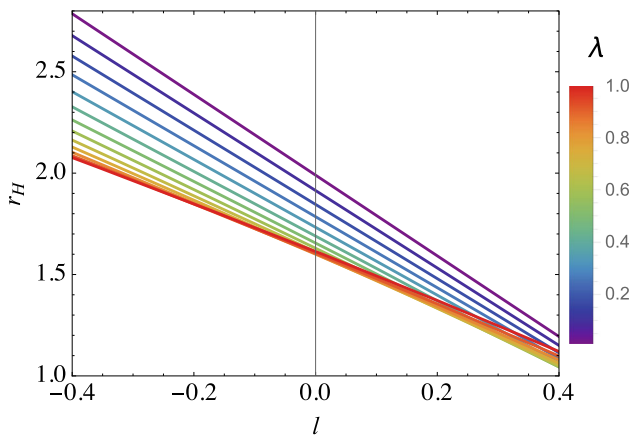


**Fig. 2** The variation of the event horizon radius of a BH in KR gravity surrounded by PFDM as a function of the parameter  $l$  for different parameter  $\lambda$

using a solution of  $f(r) = 0$ ,

$$r = \lambda(1 - l) \text{ProductLog} \left( \frac{\left( |\lambda|^{1-l} e^{\frac{2(1-l)M}{\lambda}} \right)^{\frac{1}{1-l}}}{\lambda(1-l)} \right) \quad (14)$$

where  $\text{ProductLog}(z)$ , for arbitrary  $z$ , is defined as the principal solution of the equation  $We^W = z$ .

The event horizon marks the region where the escape velocity equals the speed of light, meaning that any object crossing this boundary is inevitably drawn toward the singularity. Additional geometric and field contributions can modify the event horizon structure in KR gravity. A surrounding PFDM medium may further alter the spacetime structure near the horizon, affecting key observable features such as the photon sphere and the ISCO.

In Fig. 2, the BH’s horizon radius variation concerning the KR field parameter  $l$  is illustrated for different PFDM parameter  $\lambda$  values. From the figure, we can conclude that as the PFDM parameter  $\lambda$  increases, the event horizon begins to shrink.

### 2.2 Scalar invariants

The study of curvature invariants, including the Ricci scalar, the Ricci tensor squared, and the Kretschmann scalar, provides important information about the properties of spacetime geometric and physical properties such as stability and overall structure [15, 16]. Therefore, in this analysis, we focus on evaluating the curvature invariants to explore characteristics of the spacetime geometry of a black hole surrounded by PFDM in KR gravity in detail.

**The Ricci scalar.** First, we analyze the influence of the spacetime parameters  $\lambda$  and  $l$  on the behavior of the Ricci scalar.

The mathematical expression for the Ricci scalar can be derived explicitly as follows:

$$R = g_{\mu\nu} R^{\mu\nu} = \frac{\lambda}{r^3} + \frac{2l}{(1-l)r^2}. \quad (15)$$

One can explore how the KR and PFDM fields affect the curvature properties of spacetime on the Ricci scalar, highlighting the interplay between their contributions to spacetime curvature.

**The square of Ricci tensor.** Now, we explore the square of the Ricci tensor of the spacetime described by Eq. (13), which can be expressed in the following form:

$$R_{\mu\nu} R^{\mu\nu} = \frac{2l^2}{(1-l)^2 r^4} + \frac{4\lambda l}{(1-l)r^5} + \frac{5\lambda^2}{2r^6} \quad (16)$$

By evaluating the square of the Ricci tensor, one can examine how these parameters affect the overall curvature structure of the spacetime, providing deeper insights into its geometric properties.

**The Kretschmann scalar.** Now, we explore the Kretschmann scalar ( $\mathcal{K} = R_{\mu\nu\lambda\sigma} R^{\mu\nu\lambda\sigma}$ ,  $R_{\mu\nu\lambda\sigma}$  represents the Riemann curvature tensor), which provides additional information about the curvature of the spacetime with the radial function described by Eq. (13). It helps better understand spacetime singularities, asymptotic behavior, and other curvature features, especially in Ricci-flat geometries. Unlike the Ricci scalar, the Kretschmann scalar does not vanish even for Ricci-flat spacetimes, making it a useful quantity to get additional insights into the properties of a given Ricci-flat spacetime. The exact analytical expression for the Kretschmann scalar for the spacetime with the function (13) is,

$$\begin{aligned} \mathcal{K} = & \frac{48M^2 + 40M\lambda + 13\lambda^2}{r^6} \\ & + \frac{4l^2}{(1-l)^2 r^4} - \frac{8l}{(1-l)r^5} \left( 2M - \lambda \ln \frac{r}{|\lambda|} \right) \\ & + \frac{\lambda}{r^6} \ln \frac{r}{|\lambda|} \left[ 4\lambda \left( 3 \ln \frac{r}{|\lambda|} - 5 \right) - 48M \right]. \end{aligned} \quad (17)$$

Figure 3 illustrates the radial dependence of the scalar invariants for the different values of the PFDM parameters of  $\lambda$  for case  $l = 0.2$  in the upper panel and the Lorentz symmetry breaking parameter  $l$  for case  $\lambda = 0.1$  in the lower panel. One may see from the upper panel of Fig. 3 and Eqs. (15), (16) and (17) that increasing the PFDM parameter  $\lambda$  causes an increase in the values of Ricci scalar, the square of Ricci tensor, and the Kretschmann curvature scalar in the center of the BH with a background KR field surrounded by PFDM. In the lower panel of Fig. 3, all three scalar invariants increase as  $l$  increases.

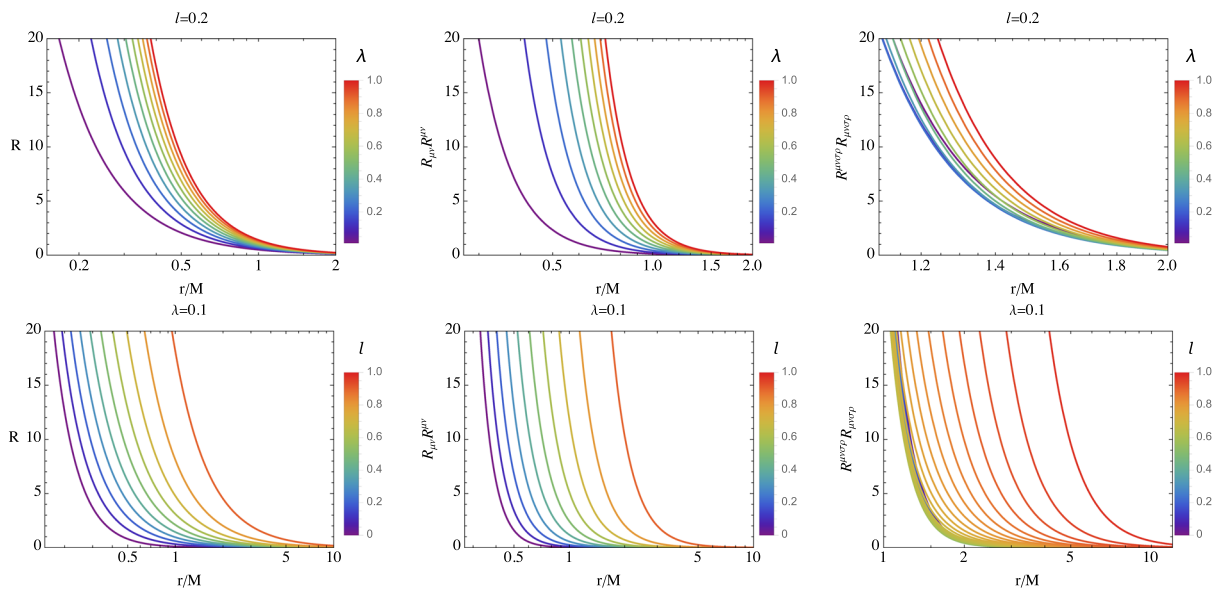


**Fig. 3** The radial profiles of scalar invariants of spacetime for various values of parameters  $\lambda$  and  $l$ . The left panel illustrates the Ricci scalar, the middle panel represents the square of the Ricci tensor, and the right panel depicts the Kretschmann scalar

### 3 Thermodynamical properties

In this section, we analyze the thermodynamic properties of a BH in KR gravity surrounded by PFDM. To achieve this, we begin by examining the event horizon. By solving the equation  $f(r) = 0$  at the event horizon, we determine the horizon radius  $r_+$ , which allows us to compute the volume of the event horizon [17,18]:

$$V = \frac{4}{3}\pi r_+^3. \tag{18}$$

To investigate this, we begin by solving the equation  $f(r_+) = 0$  for the lapse function (13) to determine the BH mass, which gives

$$M = \frac{1}{2} \left( \frac{r_+}{1-l} - \lambda \ln \frac{r_+}{|\lambda|} \right) \tag{19}$$

The first law of thermodynamics for a BH is:

$$dM = T_H dS + V dP, \tag{20}$$

where  $T_H$  is **Hawking temperature**, where  $S$  represents the entropy at the equilibrium without considering thermal fluctuation or the uncorrected entropy. Let us notice that  $S_0$ . By utilizing the given lapse function  $f(r)$ , given in Eq. (13), we can determine the temperature  $T_H$  in the following form:

$$T_H = \frac{f'(r)}{4\pi} \Big|_{r=r_+} = \frac{1}{4\pi r_+^2} \left[ 2 + \lambda \left( 1 - \ln \frac{r_+}{|\lambda|} \right) \right]. \tag{21}$$

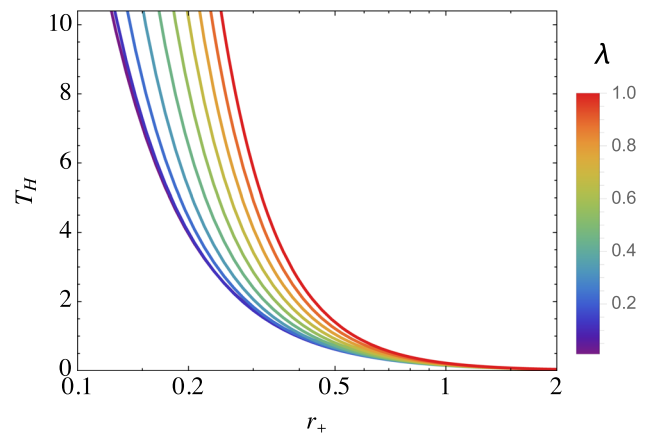


**Fig. 4** Dependence of the Hawking temperature on the BH horizon radius  $r_+$

In Fig. 4, we plot the behavior of the Hawking temperature as a function of the horizon radius for specific values of the PFDM parameter. The impact of the PFDM parameter on the Hawking temperature is evident from the diagrams. It can be inferred that increasing the  $\lambda$ -parameter leads to an increase in temperature.

**Hawking entropy.** The second law of thermodynamics for BHs is expressed as:

$$\frac{dS}{dt} \geq 0 \tag{22}$$

This law states that the entropy of a black hole never decreases; it either increases or remains constant. It is mathematically formulated using the *Bekenstein–Hawking entropy*

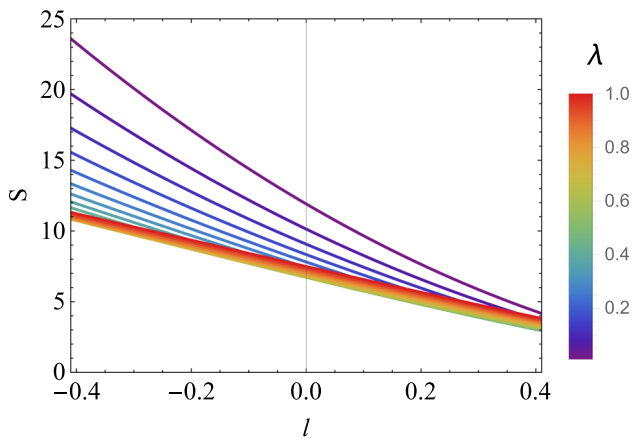


**Fig. 5** Entropy behavior for the BH in KR gravity surrounded by PFDM

equation:

$$S = \frac{k_B A}{4\hbar G} \quad (23)$$

where  $S$  is the BH entropy,  $A$  is the event horizon area,  $k_B$  is the Boltzmann constant,  $\hbar$  is the reduced Planck constant. For a spherically symmetric BH, the horizon area has the value  $A = 4\pi r_+^2$ . In geometrized units ( $k_B = 1$ ,  $\hbar = 1$ ,  $G = 1$ ), this simplifies to:

$$S = \pi r_+^2 \quad (24)$$

In Fig. 5, we have shown the characteristics of Hawking entropy. The figure shows that the entropy value increases as the PFDM parameter decreases.

**Heat capacity.** According to the third law of thermodynamics for BHs, reaching absolute zero temperature is impossible ( $T = 0$ ). In BH thermodynamics, this law implies that a BH with an extremely low temperature will asymptotically approach absolute zero over an infinite amount of time, but can never actually reach it. In other words, the temperature of an extremal BH tends to zero but never exactly reaches it. Mathematically, the temperature of a BH is,  $T_H = \frac{\kappa}{2\pi}$ , where  $T_H$  is the Hawking temperature  $\kappa$  is the surface gravity. For extremal BHs (i.e., those with the maximum possible charge or angular momentum), we have  $\kappa \rightarrow 0$ , which results in  $T_H \rightarrow 0$ . This means the temperature approaches zero but never exactly reaches it. This law is also closely related to BH evaporation and quantum effects, reinforcing that a BH can never achieve absolute zero temperature.

Now, we analyze the thermodynamic stability of the BH in KR gravity in the presence of PFDM. The heat capacity at constant volume is defined as,

$$C_V = T \frac{\partial S}{\partial T} = T \frac{\partial S}{\partial r_+} \left( \frac{\partial T}{\partial r_+} \right)^{-1}. \quad (25)$$

Plugging Eqs. (21) and (23) into (25), one finally have

$$C_V = \frac{\pi r_+^2 (2\lambda^2 - (\lambda - 2)r_+)}{(\lambda - 2)r_+ - 3\lambda^2} \quad (26)$$

The divergence of the heat capacity  $C_V$  at certain parameter combinations is indeed a critical aspect of our thermodynamic analysis, and its physical implications are consistent with well-established concepts in BH thermodynamics, particularly phase transitions. In BH thermodynamics, a divergence in heat capacity signifies a second-order phase transition. At the points of divergence, the BH ceases to be locally stable.

In the negative heat capacity case ( $C_V < 0$ ), the regions where the heat capacity is negative indicate thermodynamic instability. A BH in such a state will typically tend to either evaporate further (if it loses energy) or grow larger (if it gains energy), moving away from equilibrium. In the positive case ( $C_V > 0$ ): Regions where the heat capacity is positive signify thermodynamic stability. In these regions, the black hole can absorb or emit energy while maintaining thermal equilibrium. The points where the capacity diverges mark the boundary between these stable and unstable phases. This behavior is analogous to phase transitions in conventional thermodynamic systems, like the liquid–gas transition in a van der Waals fluid, where the specific heat diverges at the critical point. For BHs, these transitions are often interpreted as changes in the black hole’s “state”, for example, from a small, unstable BH to a large, stable one.

It is important to note that our thermodynamic analysis, deriving macroscopic quantities like temperature and entropy from the BH’s geometric properties, operates within a semi-classical framework. While we utilize established definitions such as Hawking temperature from surface gravity and Bekenstein–Hawking entropy from horizon area, a complete understanding of BH thermodynamics at a fundamental level would ideally involve the microscopic counting of underlying quantum states. The presence of the KR field, as a rank-2 antisymmetric tensor, introduces additional degrees of freedom that modify the spacetime geometry. This inherently implies a more complex set of microstates compared to vacuum black holes in GR. Similarly, the PFDM environment, which influences the metric through its energy-momentum tensor, would also affect these microstates. A detailed statistical mechanical derivation of these microstates, however, falls outside the scope of this semi-classical study and remains a profound challenge for future research in quantum gravity.

The behavior of heat capacity against horizon radius  $r_+$  was plotted in Fig. 6 for different values of the dark matter parameter  $\lambda$ . From the figure, we can conclude that as  $\lambda$  increases, the heat capacity also increases.

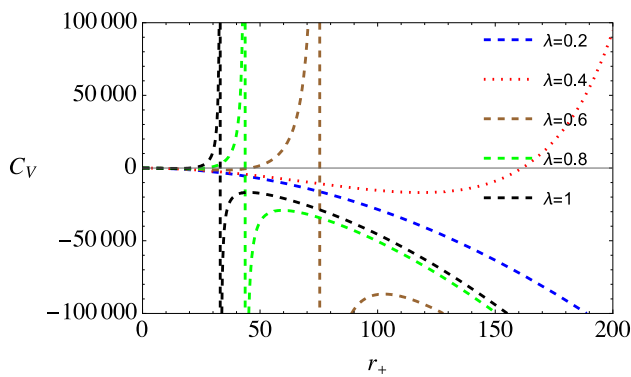


**Fig. 6** Variation of heat capacity concerning the event horizon  $r_+$  for a set of values of PFDM parameter  $\lambda$

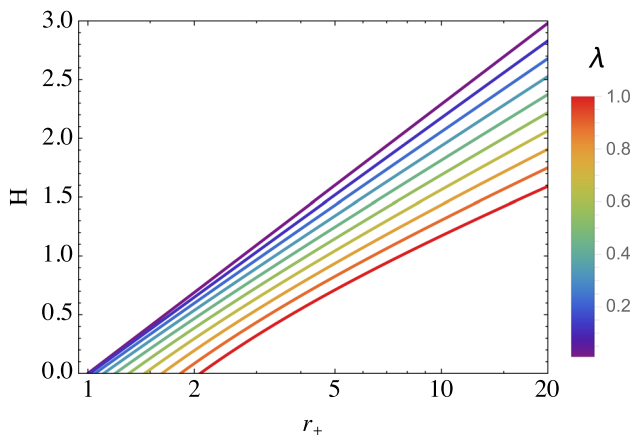


**Fig. 7** Variation of enthalpy with the BH horizon radius for various values of PFDM parameter  $\lambda$

**Enthalpy.** The enthalpy of the system is evaluated using the conventional thermodynamic equation,

$$H = \int T_H dS. \tag{27}$$

This gives the enthalpy energy of the BH surrounded by the PFDM in the KR field

$$H = \frac{1}{2} \left( (2 - \lambda) \ln r_+ - \frac{2\lambda^2}{r} \right). \tag{28}$$

In Fig. 7, the graphical characteristics of enthalpy are presented for different values of the event horizon  $r_+$  and the matter parameter  $\lambda$ . The figure shows that the enthalpy value is directly proportional to the event horizon and the PFDM parameter.

**Pressure.** In extended thermodynamics, where the mass  $M$  is interpreted as the enthalpy  $H$ , the first law is  $dM = T_H dS +$

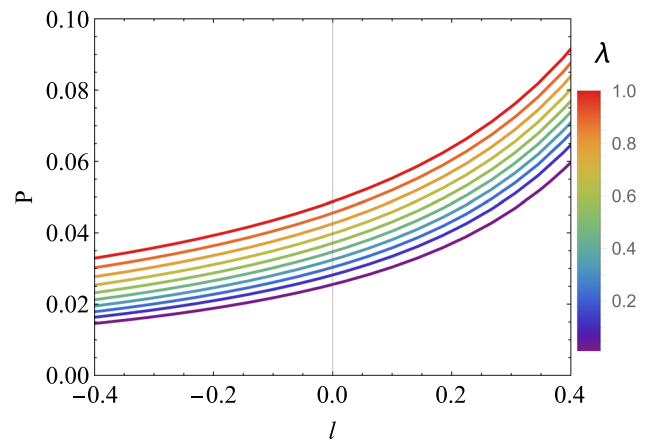


**Fig. 8** Thermodynamical pressure as a function of the parameter  $l$  for the BH in KR gravity surrounded by PFDM for different parameter values  $\lambda$

$V dP$ . Rearranging for pressure has the form,

$$P = - \left( \frac{\partial M}{\partial V} \right)_S. \tag{29}$$

Since (19) and (18), we express  $M$  as a function of  $V$  in the following form:

$$M = \frac{1}{2} \left( \lambda + \frac{\sqrt[3]{\frac{3}{\pi}} \sqrt[3]{V}}{2^{2/3}(1-l)} - \frac{2^{2/3} \sqrt[3]{\frac{\pi}{3}} \lambda^2}{\sqrt[3]{V}} \right) \tag{30}$$

The thermodynamical pressure is,

$$\frac{\partial M}{\partial V} = P = \frac{1}{6^{2/3} 2 \sqrt[3]{\pi} (1-l) V^{2/3}} + \frac{\sqrt[3]{\frac{\pi}{6}} \lambda^2}{3 V^{4/3}}. \tag{31}$$

In Fig. 8, we illustrate the graphical presentation of the thermodynamic pressure magnitude. It is observed from the figure that as the matter parameter  $\lambda$  increases, the pressure value also increases.

**Internal energy.** The above-derived quantities are used to obtain the expressions for the other system properties, such as internal energy  $U$ , Gibbs free-energy  $G$ , and specific heat  $C$  for the system of the BH in the KR field surrounded by PFDM. We use the familiar expression  $U = H - PV$  to find the internal energy, and using the expressions from (18), (28,) and (31) the internal energy and we have,

$$U = \left( 1 - \frac{\lambda}{2} \right) \ln(r_+) - \frac{1}{8\pi(1-l)(r_+^2)^{2/3}} - \frac{7\lambda^2}{6r_+} \tag{32}$$

In Fig. 9, we plotted the internal energy's dependence on the event horizon parameter for various parameter values  $\lambda$  for case  $l = 0.2$  and lorentz symmetry breaking parameter  $l$

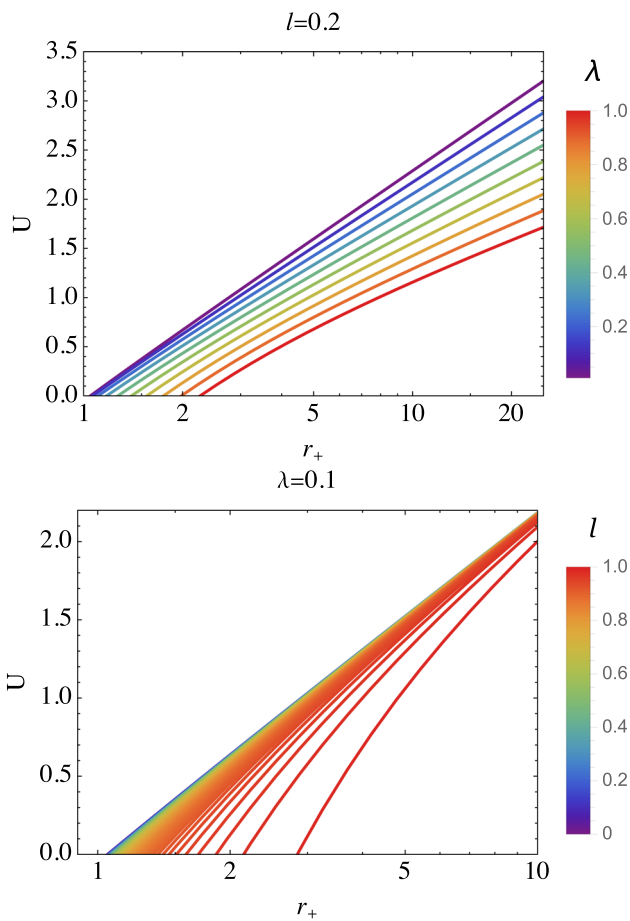


**Fig. 9** Variation of Internal energy concerning the event horizon  $r_+$  for a set of values of PFDM parameter  $\lambda$ , and lorentz symmetry breaking parameter  $l$

for case  $\lambda = 0.1$ , visually representing how these quantities interact within our model. The upper panel shows that as the  $\lambda$  parameter increases, which could be associated with specific physical properties or conditions in the system, the internal energy exhibits a corresponding decrease, suggesting a direct relationship between these two variables under the given thermodynamic framework. The lower panel shows that the internal energy decreases as the Lorentz symmetry-breaking parameter  $l$  increases.

**Gibbs free energy.** The fourth law of BH thermodynamics is often called the “Zeroth Law”, and according to the law, a stationary BH’s surface gravity ( $\kappa$ ) is constant across its event horizon. This is analogous to the Zeroth law of ordinary thermodynamics, implying a system in thermal equilibrium has a uniform temperature throughout. Similarly, the surface gravity remains uniform across the horizon for a stationary BH. Mathematically, this is expressed as  $\kappa = constant$  on the event horizon, where  $\kappa$  is the surface gravity of the BH. This law is fundamental in BH thermodynamics because surface gravity is directly related to the Hawking temperature. Thus, if a stationary BH is in equilibrium, its temperature remains

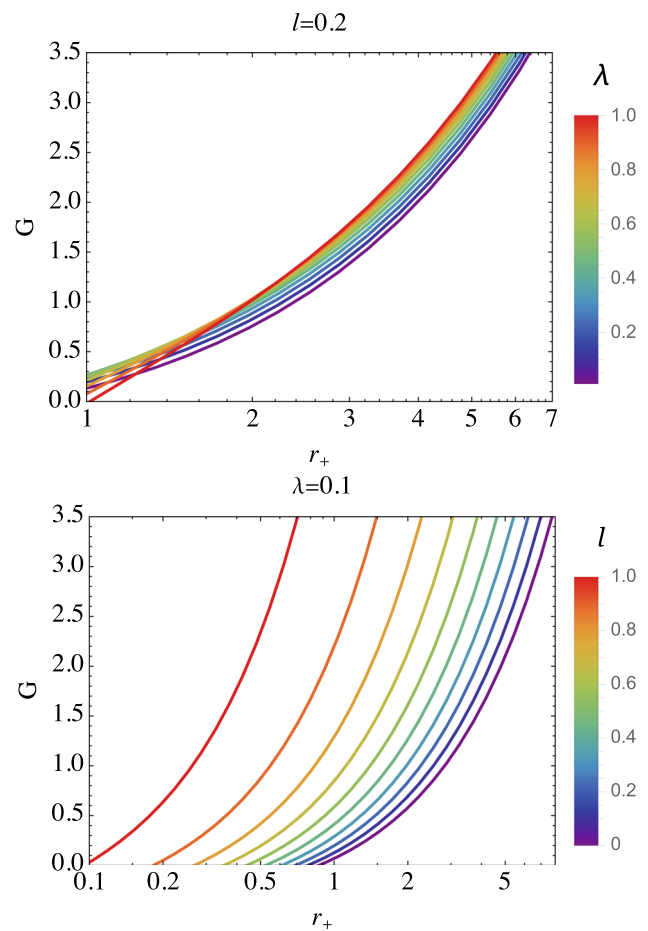


**Fig. 10** Variation of Gibbs free energy with the event horizon radius  $r_+$  for different values of PFDM parameter  $\lambda$ , and lorentz symmetry breaking parameter  $l$

uniform across the entire event horizon. Subsequently, we study the BH’s global stability characterized by the Gibbs free energy. The Gibbs free energy can be calculated using the definition  $G_+ = M_+ - T_+S_+$ , which is expressed as follows:

$$G = \frac{1}{4} \left( 3\lambda - 2 - \frac{2r_+}{l-1} - \frac{4\lambda^2}{r} \right) \tag{33}$$

Figure 10 presents a detailed graphical representation of the Gibbs free energy’s characteristics. The upper panel shows that as the PFDM parameter  $\lambda$  increases, which may correspond to changes in the dark matter density or its influence on the system, the Gibbs free energy  $G$  exhibits a noticeable decrease, implying an inverse relationship between the PFDM parameter and the Gibbs free energy. This shows how the thermodynamic properties of the system are significantly affected by variations in this parameter under the conditions specified in our model. From the lower panel, it can be seen that as Lorentz symmetry breaking  $l$  increases, the Gibbs free energy increases.

### 4 Circular motion of test particle

In this section, we explore the dynamics of test particles in the spacetime of a BH within KR gravity, surrounded by PFDM. The antisymmetric KR field and the surrounding dark matter significantly influence the spacetime geometry, modifying the particle motion [19–23].

#### 4.1 Equations of motion

The motion of a neutral test particle in the curved spherically symmetric spacetime can be analyzed using the Lagrangian approach:

$$\mathcal{L} = \frac{1}{2} g_{\mu\nu} \dot{x}^\mu \dot{x}^\nu, \tag{34}$$

where  $\dot{x}^\mu = \frac{dx^\mu}{d\tau}$ , and  $\tau$  is the proper time [24–27].

Assuming the motion of particles in the equatorial plane ( $\theta = \pi/2$ ), the Lagrangian simplifies to:

$$\mathcal{L} = \frac{1}{2} \left[ -f(r)\dot{t}^2 + \frac{\dot{r}^2}{f(r)} + r^2\dot{\phi}^2 \right]. \tag{35}$$

The conserved quantities due to the symmetries of the spacetime are

$$p_t = \frac{\partial \mathcal{L}}{\partial \dot{t}} = -f(r)\dot{t} = -\mathcal{E}, \tag{36}$$

$$p_\phi = \frac{\partial \mathcal{L}}{\partial \dot{\phi}} = r^2 \sin^2 \theta \dot{\phi} = \mathcal{L} \tag{37}$$

where,  $\mathcal{E}$  is the specific energy and  $\mathcal{L}$  is the specific angular momentum of the test particle. Using the normalization condition for massive particles  $g_{\mu\nu} \dot{x}^\mu \dot{x}^\nu = -1$ , we get:

$$-f(r)\dot{t}^2 + \frac{\dot{r}^2}{f(r)} + r^2\dot{\phi}^2 = -1. \tag{38}$$

#### 4.2 Effective potential for circular motion

The effective potential is a fundamental concept in classical and relativistic mechanics that helps describe the motion of a test particle in a given gravitational or electromagnetic field. The radial equation of motion for the test particle can be expressed as:

$$\dot{r}^2 + V_{\text{eff}}(r) = \mathcal{E}^2, \tag{39}$$

where the effective potential  $V_{\text{eff}}(r)$  is given by:

$$V_{\text{eff}}(r) = f(r) \left( 1 + \frac{\mathcal{L}^2}{r^2} \right). \tag{40}$$

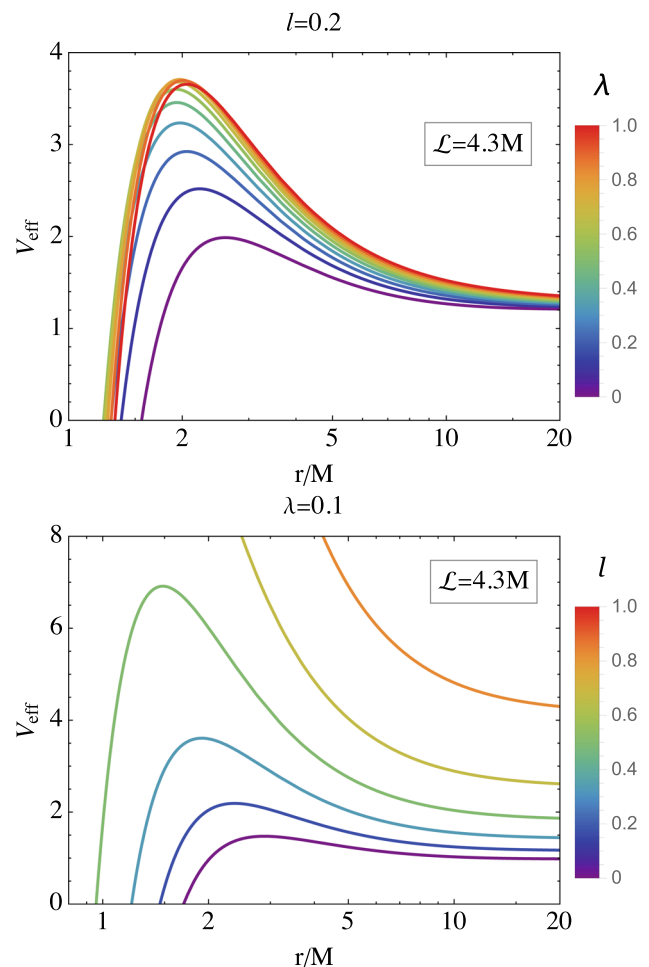


**Fig. 11** The radial dependence of test particles’ effective potential for different PFDM parameter values  $\lambda$  and Lorentz symmetry breaking parameter  $l$

The effective potential represents the contributions from the gravitational attraction and the centrifugal repulsion due to angular motion. By analyzing the effective potential, one can determine key orbital properties such as stable and unstable orbits, escape conditions, and energy thresholds for bounded motion.

Figure 11 illustrates the radial dependence of the effective potential for the radial motion of test particles for different values of the PFDM parameter  $\lambda$  in the case of  $l = 0.2$  and Lorentz symmetry breaking parameter  $l$  for case  $\lambda = 0.1$ . This graph assumes a constant specific angular momentum of  $\mathcal{L} = 4.3M$ . The upper panel illustrates that the PFDM parameter  $\lambda$  substantially impacts the effective potential. As the value of  $\lambda$  increases, the effective potential also rises, as depicted. The lower panel shows that the effective potential increases as Lorentz symmetry breaking  $l$  increases.

The minima of the effective potential correspond to stable circular orbits, where a small radial perturbation results in bounded oscillations around an equilibrium position. The maxima indicate unstable circular orbits, in which a slight

perturbation can cause the particle to fall into the central object or escape to infinity. The steepness and shape of the potential provide insights into the gravitational well and the forces governing orbital motion. For circular orbits, the following conditions must be satisfied:

$$\frac{dV_{\text{eff}}}{dr} = 0, \quad \frac{d^2V_{\text{eff}}}{dr^2} > 0. \quad (41)$$

From  $\partial_r V_{\text{eff}} = 0$ , we derive the angular momentum  $\mathcal{L}$  and energy  $\mathcal{E}$  for circular orbits as:

$$\mathcal{L}^2 = \frac{r^2 \left( \lambda \left( \ln \frac{r}{\lambda} - 1 \right) - 2M \right)}{6M - \frac{2r}{1-l} + \lambda \left( 1 - 3 \ln \frac{r}{\lambda} \right)}, \quad (42)$$

$$\mathcal{E}^2 = \frac{2 \left[ 2 \left( M - \lambda(1-l) \ln \frac{r}{\lambda} \right) - \frac{r}{1-l} \right]^2}{r \left( 6M - \frac{2r}{1-l} + \lambda \left( 1 - 3 \ln \frac{r}{\lambda} \right) \right)}. \quad (43)$$

These equations describe how the parameters  $\lambda$  and  $l$  influence the properties of circular orbits [25, 28, 29].

#### 4.3 Stable circular orbits

The second derivative of the effective potential determines the stability of circular orbits:  $\partial_r^2 V_{\text{eff}} > 0$ .

When this condition is not met, unstable circular orbits occur, indicating that the particle will spiral inward toward the BH or outward into escape trajectories.

The stability of circular orbits is critical to studying test particle dynamics around BHs in the presence of KR gravity and PFDM. Circular orbits are key indicators of the gravitational potential's nature and provide insights into the interplay between the KR field and the surrounding PFDM distribution.

To examine the stable circular orbits, one typically analyzes the effective potential,  $V_{\text{eff}}(r)$ , for a test particle. The effective potential in such a spacetime geometry is derived from the metric and includes contributions from the KR corrections and the PFDM profile [30, 31]. Stability is determined by the behavior of the second derivative of  $V_{\text{eff}}(r)$  at the location of the circular orbit [24].

Circular orbits occur at radii where the radial component of the particle's motion vanishes. Mathematically, this is given by:  $\partial_r V_{\text{eff}} = 0$ . This condition provides the radius of the circular orbit,  $r_c$ , as a function of the system's parameters, such as the BH mass, KR coupling constant, and PFDM's density profile [27].

For a circular orbit to be stable, small perturbations in the radial direction should not lead to unbounded oscillations or escape trajectories [24]. This is ensured if the second derivative of the effective potential satisfies:

$$\partial_r^2 V_{\text{eff}}|_{r=r_c} > 0. \quad (44)$$

Physically, this condition implies that the effective potential has a local minimum at  $r_c$ .

The antisymmetric KR field modifies spacetime geometry, impacting the effective potential [30]. These corrections can shift the location of stable circular orbits and alter their stability regions compared to the Schw or Kerr spacetimes [32].

The presence of PFDM adds a density-dependent term to the spacetime metric, modifying the gravitational potential [33]. Depending on the PFDM density profile (e.g., constant, power-law, or Yukawa-like distribution), circular orbits' effective potential and stability conditions can vary significantly. By numerically solving the conditions for  $\partial_r V_{\text{eff}} = 0$  and  $\partial_r^2 V_{\text{eff}} > 0$ , one can map out the stability regions in the parameter space. Key factors to analyze include the dependence of stable orbit radii on the KR coupling constant [30]. The influence of PFDM density and its distribution type on the stability criteria [31]. The comparison with standard GR predictions highlights deviations in KR gravity and PFDM induced [29]. Understanding the stable circular orbits has profound implications for astrophysical observations. Stable circular orbits are closely related to the innermost stable circular orbit (ISCO), which determines the accretion disk's inner edge. The ISCO location, modified by KR gravity and PFDM, can influence observable phenomena such as X-ray emissions and QPOs [27, 29]. Moreover, these deviations provide potential tests for alternative gravity theories and dark matter distributions using high-precision astrophysical data.

Figure 12 displays the radial distributions of the specific energy and the specific angular momentum for the circular orbits of neutral test particles around the BH in KR gravity surrounded by PFDM, considering the values of the PFDM parameter for the case  $l = 0.2$  and Lorentz symmetry breaking parameter  $l$  for case  $\lambda = 0.1$ . From the upper panel of Fig. 12, it can be concluded that the specific angular momentum decreases as the parameter  $\lambda$  increases. However, as shown in the right panel, the specific energy increases with increasing PFDM parameter  $\lambda$ . From the lower panel of Fig. 12, it can be observed that as the parameter  $l$  increases, the specific angular momentum decreases. Meanwhile, the right panel illustrates that the specific energy rises with increasing Lorentz symmetry breaking  $l$ .

#### 4.4 Minimum circular orbit

The MCO refers to a spherical region surrounding a BH where the gravitational field is intense enough to force photons (light particles) into unstable circular orbits. This expression arises from the radial extrema condition for photon orbits in general static, spherically symmetric spacetimes. This condition is described as follows: Photons travel along geodesics, which means that they move freely within the

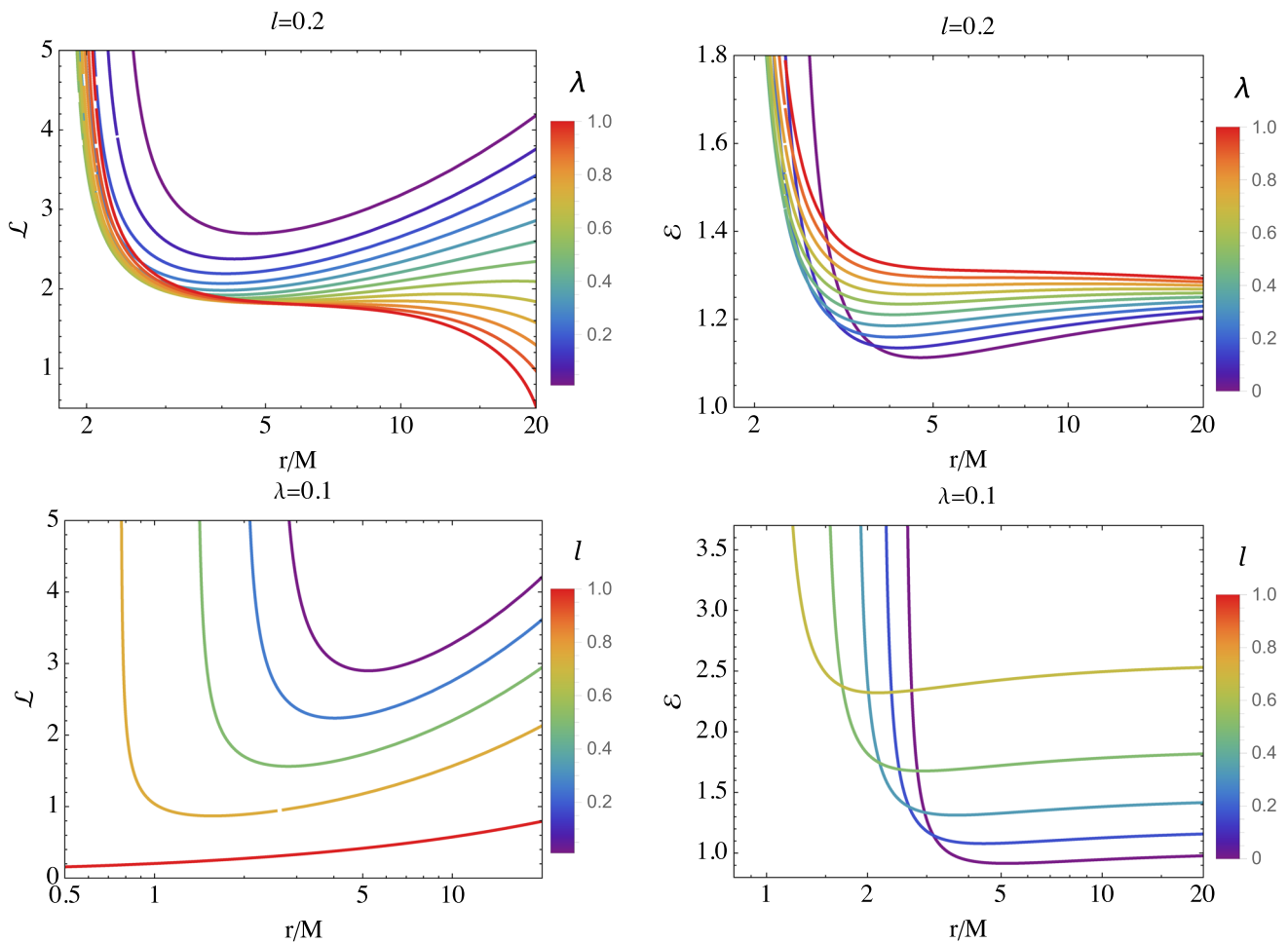


**Fig. 12** The radial dependence of specific angular momentum (left panel) and energy (right panel) for circular orbits for different values of PFDM parameter  $\lambda$  and lorentz symmetry breaking parameter  $l$

framework of the given metric. The radius must correspond to an extremum for a photon orbit to be spherical. This condition can be derived using the effective potential approach, which is written as [34,35]:

$$\left. \frac{dV_{\text{eff}}(r)}{dr} \right|_{r=r_{\text{min}}} = 0. \tag{45}$$

From the above expression, the following can be obtained:

$$6M - \frac{2r}{1-l} + \lambda \left( 1 - 3 \ln \left( \frac{r}{\lambda} \right) \right) = 0, \tag{46}$$

The photon sphere lies outside the event horizon, at a precise radius where light can orbit the BH. These orbits, however, are not stable in the long term. Any small disturbance will either pull the photon into the BH or cause it to escape into space.

Figure 13 presents the dependence of the MCO radius on the KR field parameter  $l$  for various values of the PFDM parameter  $\lambda$ . The graph shows that as the value of the PFDM parameter increases, the minimum circular orbit decreases.

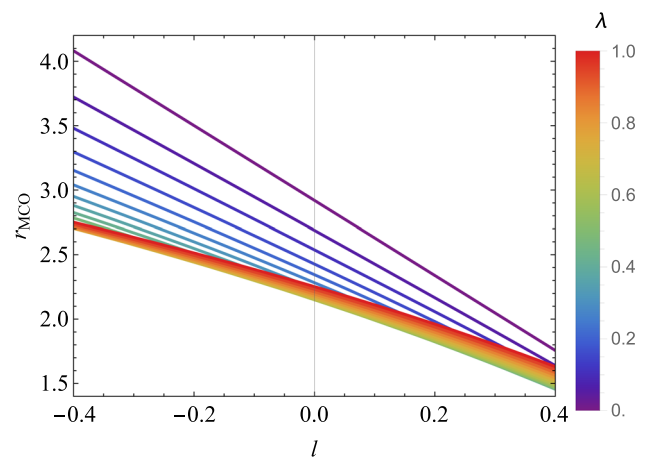


**Fig. 13** Radius of the MCO as a function of the parameter  $l$  for the BH in KR gravity surrounded by PFDM for different parameter values  $\lambda$

#### 4.5 Innermost stable circular orbits

The innermost stable circular orbit (ISCO) represents the smallest radius at which a test particle can maintain a stable

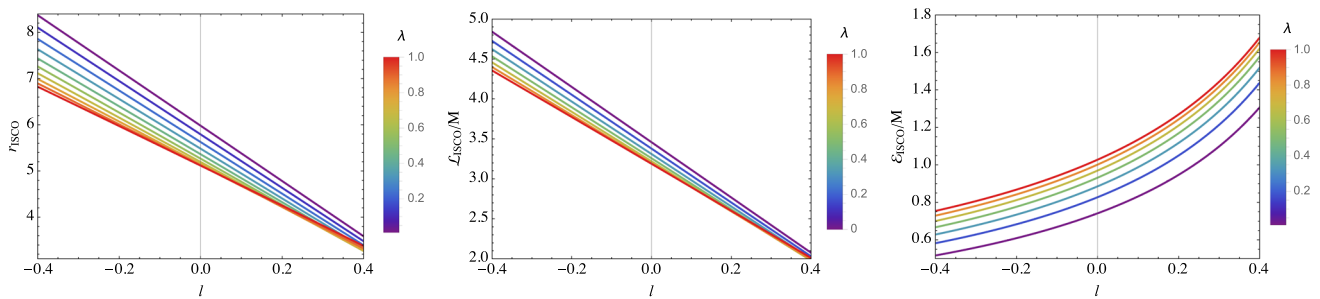


**Fig. 14** Graphical illustration of ISCO radius, the specific angular momentum, and specific energy at the ISCO radius of neutral particles for different values of the parameter  $l$

circular trajectory. Beyond the ISCO, circular orbits become unstable, leading to a transition to plunge into the BH or move outward.

In the presence of KR gravity and PFDM, the ISCO is influenced by modifications to the effective potential, which depend on both the KR coupling and the PFDM density profile. The ISCO is determined by solving the following equations simultaneously:

$$\partial_r V_{\text{eff}} = 0, \quad \partial_r^2 V_{\text{eff}} = 0. \quad (47)$$

The first condition ensures a circular orbit, while the second condition indicates the transition point between stable and unstable orbits. The KR field alters the space-time geometry. The strength of the KR coupling determines the degree of this shift, with stronger couplings generally leading to more significant deviations. The mathematical expression presented below can be systematically derived from the preceding equation following the outlined analytical procedure:

$$2M \left( 4\lambda - \frac{r}{1-l} + 6M \right) + \lambda^2 \left( 2 + 3 \ln^2 \frac{r}{|\lambda|} \right) - \lambda \ln \frac{r}{|\lambda|} \left( 4\lambda - \frac{r}{1-l} + 12M \right) = 0 \quad (48)$$

The PFDM density profile introduces additional terms in the metric that affect the effective potential. Depending on the PFDM distribution (e.g., constant or Yukawa-like), the ISCO radius may shift inward or outward. Due to enhanced gravitational effects, the ISCO can move closer to the BH in denser PFDM environments.

The ISCO radius can be computed numerically by solving the above equations for a given set of parameters. The key aspects to analyze include the variation of the ISCO radius with the KR coupling constant, the dependence of the ISCO on the density of the PFDM, and its distribution type.

The left panel of Fig. 14 shows how  $r_{\text{ISCO}}$  depends on the KR field parameter  $l$  for various parameters of the PFDM  $\lambda$ . The figure shows that the ISCO radius of a BH surrounded by PFDM in the KR field decreases as the PFDM parameter  $\lambda$  increases. The middle panel of Fig. 14 illustrates the specific angular momentum ( $\mathcal{L}_{\text{ISCO}}$ ) of the particles at the ISCO

for a BH in KR gravity surrounded by PFDM. As seen in the figure, as  $\lambda$  increases,  $\mathcal{L}_{\text{ISCO}}$  decreases. The right panel of Fig. 14 depicts the specific energy ( $\mathcal{E}_{\text{ISCO}}$ ) of particles at the ISCO. As shown in the figure,  $\mathcal{E}_{\text{ISCO}}$  increases with increasing  $\lambda$ . Comparison with standard GR predictions to identify deviations. The ISCO has significant astrophysical implications, particularly for the accretion disk dynamics. The inner edge of the accretion disk is typically located at the ISCO, which influences the emitted radiation spectrum and variability. Observations of X-ray emissions and QPOs from BH accretion disks provide a direct means to probe the ISCO. Deviations in ISCO properties due to KR gravity or PFDM offer potential tests for these theories and constraints on the dark matter distribution.

#### 4.6 Energy efficiency

The efficiency of converting the rest mass absorbed into outgoing electromagnetic radiation is a pivotal characteristic of the accretion process. This efficiency is defined as the ratio of the energy radiated by photons that escape to infinity from the disk surface to the mass-energy accretion rate onto the BH, both evaluated at infinity. Assuming all photons escape, the efficiency can be expressed via the specific energy at the ISCO:

$$\eta = 1 - \mathcal{E} \Big|_{r=r_{\text{ISCO}}} \quad (49)$$

Figure 15 shows the dependence of  $\eta$  on the KR parameter  $l$  for different PFDM parameter  $\lambda$  values. We can conclude from the graph that as the PFDM parameter  $\lambda$  increases, energy efficiency  $\eta$  decreases.

## 5 Radiation properties

In studying the radiation properties around a BH within a KR field enveloped by PFDM, we concentrate on several key features of the accretion disk: the radiant energy flux across its surface, the radiative efficiency, the temperature distribution, and the spectrum of thermally emitted radiation.

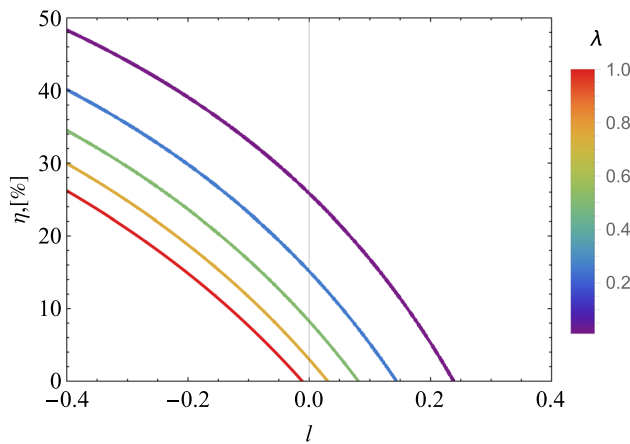


**Fig. 15** A graphical representation of the energy efficiency at the ISCO radius of neutral particles for various values of the PFDM parameter  $\lambda$

The expression describes the electromagnetic radiation flux from the accretion disk:

$$\mathcal{F}(r) = -\frac{\dot{M}_0}{4\pi\sqrt{g}} \frac{\Omega_{,r}}{(E - \Omega L)^2} \int_{r_{ISCO}}^r (E - \Omega L)L_{,r} dr. \quad (50)$$

Figure 19 illustrates the radial variation of this flux, which is influenced by different values of PFDM intensity  $\lambda$  and parameter  $l$ . From the upper panel, it can be observed that as  $\lambda$  increases, the flux decreases. Similarly, the lower panel also illustrates a decline in flux with increasing  $l$ .

Since the black body radiation flux is given by  $F = \sigma T^4$ , where  $\sigma$  is the Boltzmann constant, the disk temperature profile is illustrated in Fig. 16. From the figure, it can be seen that as the PFDM parameter  $\lambda$  increases, which may reflect alterations in the underlying dark matter dynamics or its interaction with the surrounding environment, the temperature of the accretion disk undergoes a discernible reduction. This observation points to a compelling inverse correlation between the PFDM parameter and the thermal profile of the disk. It suggests that the PFDM field's enhanced presence or influence plays a pivotal role in cooling the accretion disk, thereby profoundly impacting its radiative and thermodynamic properties.

In Fig. 17, a more detailed view of the temperature dependence on the radial distance and the PFDM parameter  $\lambda$  is provided through a density plot.

The luminosity of the emitted radiation is determined by:

$$\frac{d\mathcal{L}_\infty}{d \ln r} = 4\pi r \sqrt{g} E \mathcal{F}(r), \quad (51)$$

We assume that the emitted radiation can be described using the properties of blackbody radiation. Based on this assumption, the spectral luminosity  $\nu \mathcal{L}_{\nu, \infty}$  can be expressed as a function of the radiation frequency  $\nu$  observed at infinity.

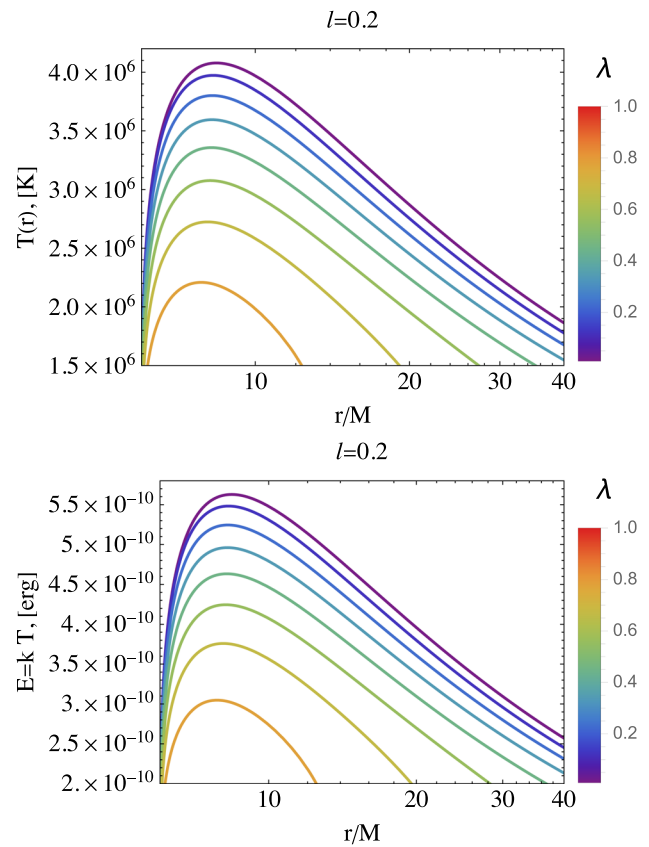


**Fig. 16** Temperature profile in Kelvin (upper panel) and energy units (lower panel)

$$\nu \mathcal{L}_{\nu, \infty} = \frac{60}{\pi^3} \int_{r_{ISCO}}^{\infty} \frac{\sqrt{g} E}{M_T^2} \frac{(u^t y)^4}{\exp\left[\frac{u^t y}{(M_T^2 \mathcal{F})^{1/4}}\right] - 1} dr \quad (52)$$

where  $i$  is the angle of inclination of the disk,  $r_{ISCO}$  and  $r_\infty$  are the inner and outer edges, and  $I(\nu)$  is the Planck distribution function. The emitted frequency,  $\nu_e = \nu(1 + z)$ , includes a redshift factor  $z$ , given by:

$$1 + z = \frac{1 + \Omega r \sin \phi \sin i}{\sqrt{-g_{tt} - \Omega^2 g_{\phi\phi}}}, \quad (53)$$

Figure 18 illustrates the radiation spectrum ( $r d\mathcal{L}_\infty / dr$ ) of the accretion disk around the BH surrounded by PFDM in KR gravity as a function of the radial coordinate  $r$ , for different fixed values of the PFDM intensity parameter  $\lambda$ , highlighting the influence of PFDM on the radiation. The curves demonstrate that increasing the PFDM ( $\lambda$ ) reduces the maximum luminosity and maximum in the spectrum shift toward lower frequencies, consistent with the decrease in temperature and radiant energy flux as also observed in Figs. 19 and 16, due to the outward shift of the ISCOs, as detailed in Fig. 14. The results provide a distinctive observational signature to test

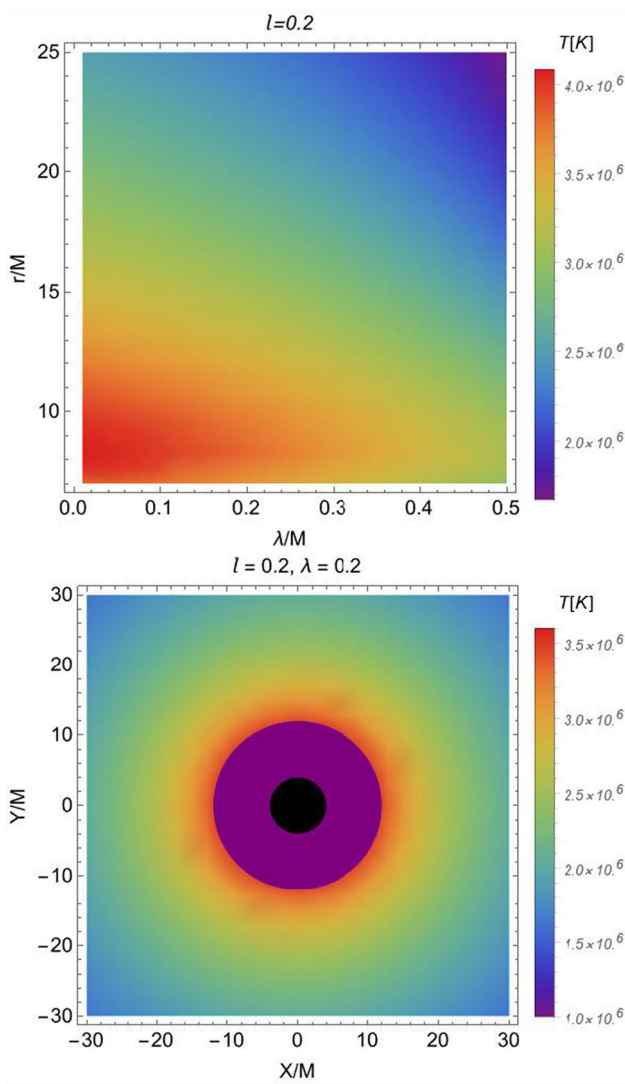


**Fig. 17** Upper panel: Temperature density plot vs. radius and  $\lambda$ . Lower panel: Profile for  $\lambda = 0.2$

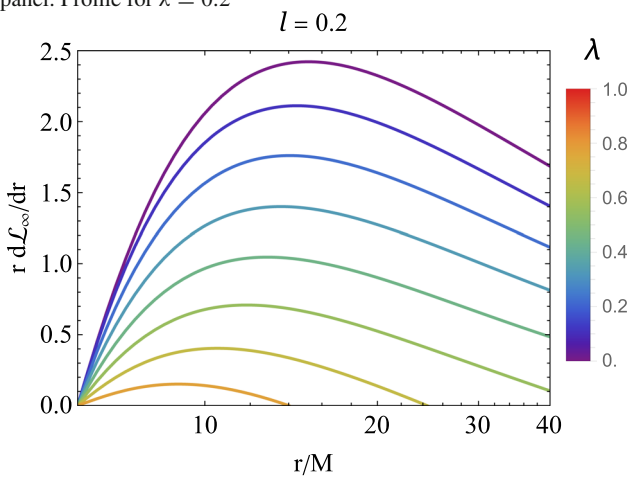


**Fig. 18** Radiation spectrum for fixed PFDM intensity values

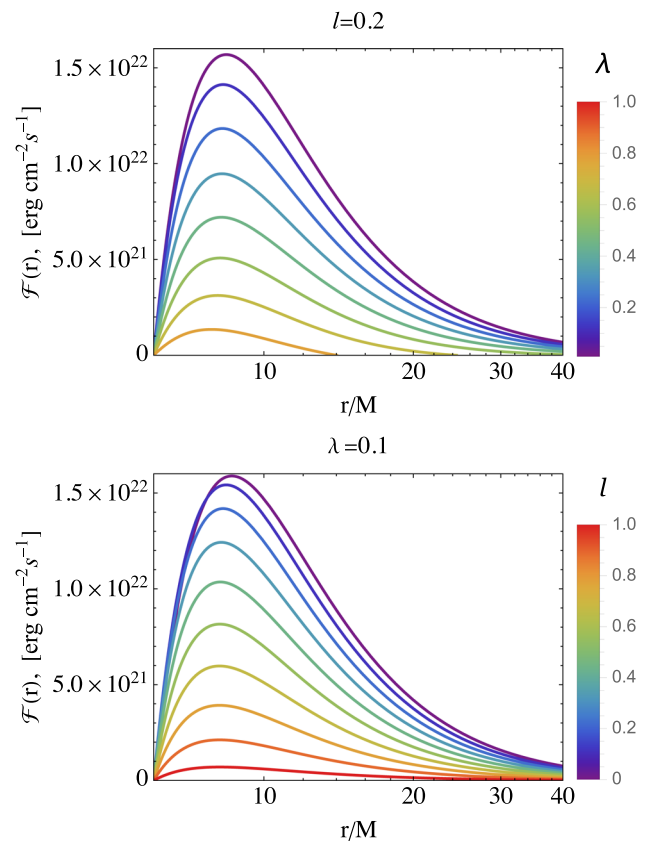


**Fig. 19** Radial variation of radiant energy flux with PFDM intensity  $\lambda$  and lorentz symmetry breaking parameter  $l$

the KR field's and PFDM's combined effects against standard GR predictions.

### 6 Fundamental frequencies

The motion of test particles in the spacetime around BHs can be decomposed into radial, azimuthal, and vertical oscillations. The frequencies associated with these oscillations, known as fundamental frequencies, are essential to understanding the dynamics of accretion disks and the origin of QPOs. In the presence of KR gravity and PFDM, the fundamental frequencies are modified due to changes in the spacetime geometry. The three fundamental frequencies are:

#### 6.1 Keplerian frequency

The Keplerian frequency,  $\nu_K$ , is a fundamental frequency associated with the orbital motion of a test particle around a central massive object. It describes the azimuthal angular velocity of the particle along a stable circular orbit and is crucial to understanding the dynamics of the accretion disk and the QPO phenomenon. In the context of a general spacetime metric influenced by KR gravity and PFDM, the Keplerian frequency is given by:

$$\nu_{K,r,\theta} = \frac{1}{2\pi} \frac{c^3}{GM} \Omega_{\phi,r,\theta}, [\text{Hz}]. \tag{54}$$

The KR field modifies the spacetime geometry, which can lead to shifts in the Keplerian frequency. These modifications depend on the field coupling constant. The PFDM profile introduces additional terms to the metric, which alter the gravitational potential. Depending on the density distribution of PFDM, the Keplerian frequency may deviate from its standard form. The Keplerian frequency plays a pivotal role in explaining the orbital motion of matter in accretion disks and the observed QPOs in BH systems. Deviations in  $\nu_K$  due to KR gravity and PFDM directly probe these effects, offering potential tests for alternative gravity theories and dark matter profiles.

Azimuthal frequency ( $\Omega_\phi$ ), which is the frequency of Keplerian orbits of test particles in the azimuthal direction, is given by,

$$\Omega_\phi = \frac{d\phi}{dt} = \frac{M}{r^3} + \frac{\lambda}{2r^3} \left( 1 - \ln \frac{r}{|\lambda|} \right). \tag{55}$$

### 6.2 Radial and vertical oscillations

Radial and vertical frequencies ( $\Omega_r$  and  $\Omega_\theta$ ) are the frequency of oscillations of the particles in the radial direction along the stable orbits, which can be determined from the second derivatives of the effective potential by radial and  $\theta$  coordinates:

$$\Omega_r^2 = \frac{1}{2g_{rr}(u^t)^2} \left. \frac{\partial^2 V_{\text{eff}}}{\partial r^2} \right|_{r=r_c} \tag{56}$$

and

$$\Omega_\theta^2 = \frac{1}{2g_{\theta\theta}(u^t)^2} \left. \frac{\partial^2 V_{\text{eff}}}{\partial \theta^2} \right|_{r=r_c}, \tag{57}$$

respectively.

The KR field and PFDM density profile alter the spacetime geometry, affecting the fundamental frequencies. These modifications can shift the values of  $\Omega_\phi$ ,  $\Omega_r$ , and  $\Omega_\theta$ ; influence the resonance conditions that give rise to QPOs; and provide observational signatures to test the presence of PFDM and the effects of KR gravity.

$$\Omega_r^2 = \Omega_\phi^2 \left\{ \frac{1}{1-l} - \frac{6M}{r} - \frac{\lambda}{r} \left[ 1 + 3 \ln \frac{r}{|\lambda|} + \frac{\lambda(1-l) + r}{2M + \lambda \left( 1 + \ln \frac{r}{|\lambda|} \right)} \right] \right\}. \tag{58}$$

Fundamental frequencies are directly linked to QPOs observed in X-ray binaries and active galactic nuclei. Determination in these frequencies compared to predictions from

GR can constrain alternative theories of gravity and dark matter distributions.

This section will derive the fundamental frequency expressions for test particles orbiting BHs in KR gravity with surrounding PFDM. This model provides a straightforward explanation of QPO observations around compact astrophysical objects.

## 7 QPO applications

QPOs are fundamental features observed in the X-ray spectra of accreting matter around BHs and other compact objects. These oscillations, characterized by their periodic or quasi-periodic nature, are invaluable diagnostic tools, with their frequencies often linked to physical processes occurring near the event horizon or within the accretion disk. Recent high-precision X-ray observatories, such as NICER, have significantly advanced QPO studies by providing unprecedented data on their spectral characteristics and variability. The forthcoming enhanced X-ray Timing and Polarimetry mission (eXTP) is poised to offer even deeper insights into strong gravity regimes and accretion phenomena, which are critical for testing alternative gravitational theories. In the context of test particles orbiting BHs in KR gravity surrounded by PFDM, several models can be proposed to explain the observed QPOs. The modeling of QPOs in modified gravitational theories, such as KR gravity, requires careful consideration of the various perturbative processes that govern particle dynamics. The RP model model posits that QPOs originate from the precession of test particle orbits within the (strong) gravitational field of a central BH. In the context of KR gravity, additional field components modify these precession rates and the orbital parameters of test particles. The introduction of a PFDM environment further influences the orbital motion, potentially changing the precession frequency depending on the fluid’s density and equation of state. This model predicts QPO frequencies corresponding to the relativistic motion of particles near the ISCO (as an inner edge of the BH accretion disc) and the subsequent resonances arising from orbital instabilities. Crucially, the gravitational effects of the dark matter and the KR field can modify the location of the ISCO, in turn, this modification may lead to observable shifts in QPO frequencies. The upper frequency is given by  $\nu_U = \nu_\phi$  while the lower frequency is expressed as  $\nu_L = \nu_\phi - \nu_r$ .

Figure 20 illustrates the potential relationships between the upper and lower frequencies of twin-peak QPOs around BHs in KR gravity surrounded by PFDM, based on the RP model. In the numerical calculations, we have considered BHs with a mass of  $10M_\odot$  for the stellar mass. These plots display the potential values of upper and lower frequencies for the 3:2, 4:3, and 5:4 frequency ratios.

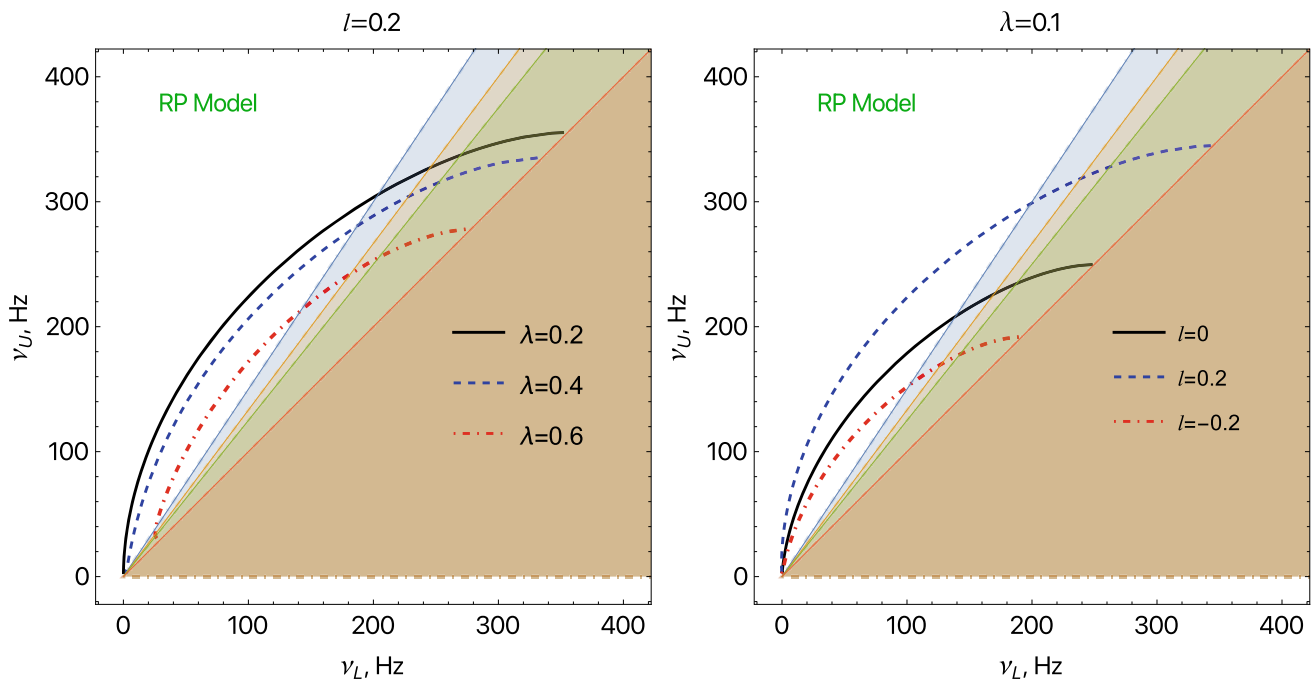


**Fig. 20** Relations between the frequencies of upper and lower picks of twin peak QPOs around BH in the KR gravity in the RP for different values of  $\lambda$  and Lorentz symmetry breaking  $l$

### 7.1 Monte Carlo Markov Chain (MCMC) priors for BHs parameters

The present section is devoted to deriving constraints on the mass and metric parameters given by the expressions (13). Here, we select three different BH candidates. The BHs depend on the mass of different classes: stellar mass, intermediate mass, and supermassive BHs. For example, we utilized well-known stellar mass BHs at the center of the microquasars GRO J1655-40 and XTE 1550-564. QPO data from (ii) M82 X-1 were also used [36]. The intermediate-mass black hole in the ultraluminous X-ray source in galaxy M82. In the literature [37, 38], it is estimated to have a mass of about 100 - 1000 solar masses. We also focus on microsecond QPOs related to the supermassive BH Sgr A\*. We employ the Python library `emcee` [39–41] to get the constraints, we then perform MCMC analysis in the RP model. The posterior distribution is [42],

$$\mathcal{P}(\theta|\mathcal{D}, \mathcal{M}) = \frac{P(\mathcal{D}|\theta, \mathcal{M}) \pi(\theta|\mathcal{M})}{P(\mathcal{D}|\mathcal{M})}, \tag{59}$$

where the functions:  $\pi(\theta)$  is the prior function and  $P(\mathcal{D}|\theta, \mathcal{M})$  is the likelihood one. We consider priors to have a normal distribution known as a Gaussian distribution within suitable boundaries (see Tables 2 and 3), *i.e.*,  $\pi(\theta_i) \sim \exp\left[-\frac{1}{2}\left(\frac{\theta_i - \theta_{0,i}}{\sigma_i}\right)^2\right]$ ,  $\theta_{low,i} < \theta_i < \theta_{high,i}$ . Here, the parameters are  $\theta_i = \{M, l, \lambda, r\}$  and  $\sigma_i$  are their deviations. We provide MCMC analysis using the orbital, vertical, and radial frequencies calculated in the previous section. The likelihood

function  $\lambda$  has form,

$$\log \lambda = \log \lambda_U + \log \lambda_L, \tag{60}$$

where  $\log \lambda_U$  denotes the likelihood of the upper and lower frequencies,

$$\log \lambda_U = -\frac{1}{2} \sum_i \frac{(v_{\phi,obs}^i - v_{\phi,th}^i)^2}{(\sigma_{\phi,obs}^i)^2}, \tag{61}$$

where  $\log \lambda_L$  is the probability (likelihood) of the lower frequency data.

$$\log \lambda_L = -\frac{1}{2} \sum_i \frac{(v_{L,obs}^i - v_{L,th}^i)^2}{(\sigma_{L,obs}^i)^2}, \tag{62}$$

Here  $v_{\phi,obs}^i, v_{L,obs}^i$  are direct observational results of the orbital/Keplerian frequencies ( $\nu_K$ ), periastron precession frequencies  $\nu_L = \nu_K - \nu_r$  for the source of our interest. On the other hand,  $v_{\phi,th}^i, v_{L,th}^i$  are the respective theoretical estimations.

We chose data from QPOs observed in X-ray binaries: GRO J1655-40, XTE J1550-564, M82 X-1, and Sgr A\* with well-reported observational results, as presented in Table 1.

Next, we perform the MCMC simulation to constrain the parameters ( $M, l, \lambda, r$ ) for BHs in KR gravity surrounded by PFDM. We use Gaussian priors based on parameter values from the existing literature on QPO data processing. We sampled approximately  $10^5$  points from a prior Gaussian distribution for each parameter. This allowed us to explore the

**Table 1** Frequencies of twin peak QPOs in microquasars and Galactic centre

Source [1, 11, 43–46]	$\nu_U$ [Hz]	$\Delta\nu_U$ [Hz]	$\nu_L$ [Hz]	$\Delta\nu_L$ [Hz]	Mass [1, 47, 48] [ $M_\odot$ ]
XTE J1550-564	276	$\pm 3$	184	$\pm 5$	$12.4^{+2.0}_{-1.8}$
GRO J1655-40	451	$\pm 5$	298	$\pm 4$	$5.4 \pm 0.3$
M82 X-1	5.07	$\pm 0.06$	3.32	$\pm 0.06$	$415 \pm 63$
Sgr A*	1.445	$\pm 0.16$ mHz	0.886	$\pm 0.04$ mHz	$(4.1 \pm 0.6) \times 10^6$

**Table 2** The Gaussian priors ( $\mu$  is the mean value and  $\sigma$  the variance) of the KR from QPOs of the sources with positive values of  $l$

$P$	XTE J1550-564		GRO J1655-40		M82 X-1		Sgr-A*	
	$\mu$	$\sigma$	$\mu$	$\sigma$	$\mu$	$\sigma$	$\mu$	$\sigma$
$M/M_\odot$	11.3159	1.4711	5.3366	0.6937	411.959	53.55	$3.7219 \times 10^6$	$0.4838 \times 10^6$
$l$	0.2507	0.0325	0.1487	0.0188	0.0430	0.0056	0.4743	0.0617
$\lambda/M$	0.0399	0.0038	0.0055	0.0007	0.0398	0.0051	0.0401	0.0052
$r/M$	4.6391	0.6031	5.6044	0.7285	6.0244	0.7832	3.2208	0.4187

**Table 3** Best fit values of  $M$ ,  $l$ ,  $\lambda/M$ , and  $r$  parameters for XTE J1550-564, GRO J1655-40, Sgr A\* and M82 X-1

$P$	XTE J1550-564	GRO J1655-40	M82 X-1	Sgr A*
$M/M_\odot$	$11.3176^{+0.7093}_{-0.6678}$	$5.3498^{+0.2128}_{-0.2033}$	$413.093^{+10.916}_{-10.805}$	$(3.7086^{+0.4545}_{-0.4400}) \times 10^6$
$l$	$0.2496^{+0.0270}_{-0.0275}$	$0.1444^{+0.0177}_{-0.0178}$	$0.0430^{+0.0055}_{-0.0056}$	$0.4710^{+0.0455}_{-0.0477}$
$\lambda/M$	$0.0300^{+0.0038}_{-0.0038}$	$0.0056^{+0.0007}_{-0.0007}$	$0.0398^{+0.0051}_{-0.0051}$	$0.0401^{+0.0052}_{-0.0052}$
$r/M$	$4.6503^{+0.1876}_{-0.1811}$	$5.6088^{+0.1344}_{-0.1323}$	$6.0278^{+0.0846}_{-0.0814}$	$3.2665^{+0.2411}_{-0.2364}$

physically possible parameter space within set boundaries and identify the best-fitting parameter values.

Having established the priors, we use the available data to perform an MCMC simulation to determine the plausible range of the parameters  $\{M, l, \lambda, r\}$  for the BH spacetime. Considering the Gaussian prior distribution, we sample  $1 \times 10^5$  points for every parameter. This approach allows us to investigate the physically allowed multidimensional parameter space within defined limits and obtain the parameter values that best match the data.

In Fig. 21, we show the results of the MCMC analysis of the KR gravity parameter by using the QPO data from 4 different charged BHs (two stellar-mass BH candidates, one intermediate-mass BH, and supermassive BHs). We use the *emcee* package to obtain the posterior distribution with the possible choice of the prior given in Tables 2 and 3. In the analysis, the contour plots highlight the confidence levels ( $1\sigma$  for 68%,  $2\sigma$  for 95%, and  $3\sigma$  for 99%) of the posterior probability distributions for the entire set of parameters. The shaded regions on the contour plots reflect these confidence levels.

## 8 Conclusion

In this study, we have investigated the spacetime properties of BHs embedded in a PFDM environment within the framework of KR gravity. First, we have derived a novel metric

incorporating the KR field and dark matter effects, characterized by the unique lapse function that distinguishes it from standard solutions in GR. We have also performed analyses of scalar invariants such as the Ricci scalar, Ricci tensor squared, and Kretschmann scalar that confirmed the significant influence of both the PFDM and the KR field parameters, revealing the contribution of curvature near the BH horizon.

Our thermodynamic analysis has explored the effects of the KR field and PFDM on key properties like Hawking temperature, entropy, heat capacity, and Gibbs free energy. The findings demonstrate that increased PFDM density or KR coupling parameters systematically affect the thermodynamic stability of the BH, influencing its entropy, temperature, and heat capacity. These modifications lead to distinctive thermodynamic signatures, indicating potential phase transitions and shifts in BH stability conditions compared to GR.

We further studied the circular motion of test particles around the BH, identifying the conditions for stable orbits through effective potential analysis. The presence of KR fields and PFDM notably alters the orbital parameters, including the radii of stable circular orbits, specific energy, and angular momentum. These effects extend to critical astrophysical parameters like the ISCO and MCO, impacting observable phenomena such as accretion disk properties and energy extraction efficiency from BH accretion processes.

The following main results are obtained:

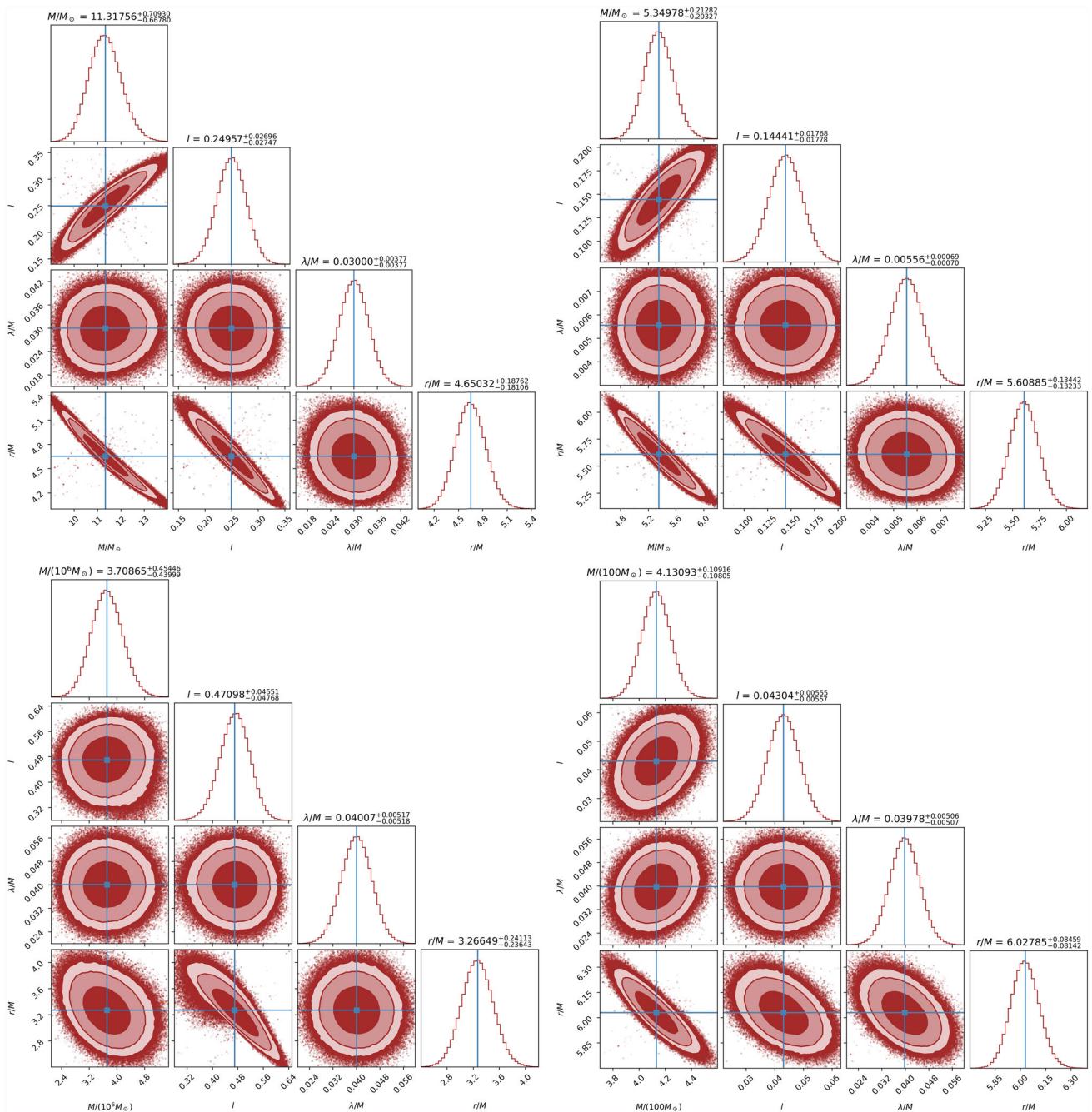


**Fig. 21** Constraints on charged BH parameters in the KR gravity, of the QPO orbit from a four-dimensional MCMC analysis using the QPO data for the stellar-mass BHs XTE J1550-564 (top left) and GRO J1655-40

(top right), supermassive BH Sgr A\* (bottom left), and intermediate-mass M82 X-1 (bottom right) in the RP model

- the effective potential governing the motion of test particles is significantly affected by both the PFDM and the Lorentz symmetry-breaking parameters;
- for circular orbits, the specific angular momentum of test particles decreases with an increase in the PFDM parameter, while the specific energy increases with the PFDM parameter;

- the radius of the minimum circular orbit (MCO) decreases as the PFDM parameter ( $\lambda$ ) increases;
- The ISCO radius of the BH also decreases with an increase in the PFDM parameter;
- at the ISCO, the specific angular momentum of particles decreases, and the specific energy increases as the PFDM parameter ( $\lambda$ ) increases;

- The energy conversion efficiency in the accretion process depends on the KR parameter ( $l$ ) and the PFDM parameter ( $\lambda$ ).

Radiation properties from accretion disks around BHs were also investigated. The results revealed that PFDM and the KR field significantly affect radiative flux, temperature distributions, and emitted radiation spectra. Increasing PFDM density generally decreased radiation flux and cooler disk temperatures, providing observable distinctions from standard gravitational models. Results show that:

- the radiant energy flux from the surface of the accretion disk decreases with increasing values of both the PFDM intensity parameter ( $\lambda$ ) and the parameter ( $l$ );
- The temperature of the accretion disk shows a discernible reduction as the PFDM parameter ( $\lambda$ ) increases. This suggests an inverse relationship where a stronger presence or influence of the PFDM field leads to a cooling effect on the accretion disk;
- The accretion disk's radiation spectrum is affected by the PFDM intensity ( $\lambda$ ). The maximum luminosity decreases as the PFDM intensity increases, and the spectrum's peak shifts toward lower frequencies. This is consistent with the observed decrease in temperature and radiant energy flux due to the outward shift of the ISCO. These findings provide a distinctive observational signature that can be used to test the combined effects of the KR field and PFDM against standard general relativity predictions.

Additionally, we have analyzed QPOs through fundamental frequencies related to radial, vertical, and azimuthal oscillations of particles in orbit around BHs. The KR and PFDM parameters introduce apparent deviations in these frequencies, allowing distinct observational signatures to be tested through X-ray spectral analysis.

The presence of the KR field and PFDM modifies the spacetime geometry, which affects the fundamental frequencies of test particles, including the Keplerian frequency, radial oscillation frequency, and vertical oscillation frequency. These modifications can cause shifts in the values of these fundamental frequencies compared to those predicted by standard GR. In turn, changes in these frequencies can influence the resonance conditions believed to be the origin of QPOs observed in the X-ray spectra of the black hole accretion disc. Deviations in the fundamental frequencies from the predictions of GR provide potential observational signatures of alternative theories of gravity and constrain the properties of dark matter distributions.

Next, we have focused on the applications of the fundamental frequencies to explain QPOs observed in black hole systems. We used the RP model, which is proposed as a framework to understand the observed QPOs in the X-ray

spectra of accreting matter around the black hole. This model relates the upper and lower frequencies of twin-peak QPOs to test particles' orbital and radial frequencies. Finally, MCMC analysis was performed using the RP model and observational data from four black hole candidates: XTE J1550-564, GRO J1655-40, M82 X-1, and Sgr A\*. The MCMC analysis aimed to constrain these BHs' mass and metric parameters, including the KR gravity parameter, using the observed QPO frequencies.

Astrophysically, this work emphasizes the importance of considering alternative gravity theories combined with dark matter environments to better understand the behavior and observational characteristics of BH systems. Our findings indicate potential observational tests using QPOs and radiation spectra, offering novel ways to constrain or support modified gravity theories and dark matter distributions. Future studies will extend this approach by incorporating more realistic astrophysical scenarios, including detailed numerical simulations and comparisons with observational data from various BH candidates.

**Data Availability Statement** This manuscript has no associated data. [Author's comment: This paper is a pure theoretical study, and no associated code/software is involved.]

**Code Availability Statement** This manuscript has no associated code/software. [Author's comment: Code/Software sharing not applicable to this article as no code/software was generated or analysed during the current study.]

**Open Access** This article is licensed under a Creative Commons Attribution 4.0 International License, which permits use, sharing, adaptation, distribution and reproduction in any medium or format, as long as you give appropriate credit to the original author(s) and the source, provide a link to the Creative Commons licence, and indicate if changes were made. The images or other third party material in this article are included in the article's Creative Commons licence, unless indicated otherwise in a credit line to the material. If material is not included in the article's Creative Commons licence and your intended use is not permitted by statutory regulation or exceeds the permitted use, you will need to obtain permission directly from the copyright holder. To view a copy of this licence, visit <http://creativecommons.org/licenses/by/4.0/>.

Funded by SCOAP<sup>3</sup>.

## References

1. R.A. Remillard, J.E. McClintock, *Annu. Rev. Astron. Astrophys.* **44**, 49 (2006). <https://doi.org/10.1146/annurev.astro.44.051905.092532>. [arXiv:astro-ph/0606352](https://arxiv.org/abs/astro-ph/0606352) [astro-ph]
2. J. Rayimbaev, N. Juraeva, M. Khudoyberdiyeva, A. Abdujabbarov, M. Abdullaev, *Galaxies* **11**, 113 (2023). <https://doi.org/10.3390/galaxies11060113>
3. M. Kalb, P. Ramond, *Phys. Rev. D* **9**, 2273 (1974). <https://doi.org/10.1103/PhysRevD.9.2273>
4. W.F. Kao, W.B. Dai, S.-Y. Wang, T.-K. Chyi, S.-Y. Lin, *Phys. Rev. D* **53**, 2244 (1996). <https://doi.org/10.1103/PhysRevD.53.2244>

5. Z.-Q. Duan, J.-Y. Zhao, K. Yang, Eur. Phys. J. C **84**, 798 (2024). <https://doi.org/10.1140/epjc/s10052-024-13188-5>. arXiv:2310.13555 [gr-qc]
6. V. Kiselev, Class. Quantum Gravity **20**, 1187 (2003). <https://doi.org/10.1088/0264-9381/20/6/310>
7. X. Hou, Z. Xu, J. Wang, J. Cosmol. Astropart. Phys. **2018**, 040 (2018). <https://doi.org/10.1088/1475-7516/2018/12/040>. arXiv:1810.06381 [gr-qc]
8. R.A. Remillard, J.E. McClintock, Annu. Rev. Astron. Astrophys. **44**, 49 (2006). <https://doi.org/10.1146/annurev.astro.44.051905.092532>
9. J. Rayimbaev, S. Jumaniyozov, M. Umaraliyev, A. Abdujabbarov, Universe **8**, 496 (2022). <https://doi.org/10.3390/universe8100496>
10. M.A. Abramowicz, W. Kluzniak, Astron. Astrophys. **374**, L19 (2001). <https://doi.org/10.1051/0004-6361:20010791>
11. S. Jumaniyozov, S.U. Khan, J. Rayimbaev, A. Abdujabbarov, S. Urinbaev, S. Murodov, Eur. Phys. J. C **84**, 964 (2024). <https://doi.org/10.1140/epjc/s10052-024-13351-y>
12. J. Rayimbaev, S. Shaymatov, M. Jamil, Eur. Phys. J. C **81**, 699 (2021). <https://doi.org/10.1140/epjc/s10052-021-09488-9>. arXiv:2107.13436 [gr-qc]
13. S. Jumaniyozov, M. Zahid, M. Alloqulov, I. Ibragimov, J. Rayimbaev, S. Murodov, Eur. Phys. J. C **85**, 126 (2025). <https://doi.org/10.1140/epjc/s10052-025-13863-1>
14. A. Einstein, Sitzungsberichte der Preussischen Akademie der Wissenschaften zu Berlin **84**, 769–822 (1915). <https://doi.org/10.1002/andp.19163540702>
15. E. Poisson, *A Relativist's Toolkit: The Mathematics of Black-Hole Mechanics* (Cambridge University Press, Cambridge, 2004). <https://doi.org/10.1017/CBO9780511606601>
16. C. Cherubini et al., Int. J. Mod. Phys. D **11**, 827 (2002). <https://doi.org/10.1142/S0218271802002037>
17. A. Ditta, F. Javed et al., J. High Energy Astrophys. **45**, 62 (2025). <https://doi.org/10.1016/j.jheap.2024.11.010>
18. H.G. Mert Mangut, I. Sakalli, Chin. Phys. C **49**, 065106 (2025). <https://doi.org/10.1088/1674-1137/adbacf>
19. A. Einstein, Sitzungsber. Preuss. Akad. Wiss. Berlin (Math. Phys.) **1915**, 844 (1915)
20. S. Hossenfelder, Living Rev. Relativ. **16** (2012). <https://doi.org/10.12942/lrr-2013-2>
21. S. Jumaniyozov, S. Khan, J. Rayimbaev et al., Eur. Phys. J. C **84**, 291 (2024). <https://doi.org/10.1140/epjc/s10052-024-12605-z>
22. T.W.B. Kibble, J. Phys. A **9**, 1387 (1976). <https://doi.org/10.1088/0305-4470/9/8/029>
23. A. Araújo Filho, J. Cosmol. Astropart. Phys. **2025**, 076 (2025). <https://doi.org/10.1088/1475-7516/2025/04/076>
24. S. Chandrasekhar, *The Mathematical Theory of Black Holes* (Oxford University Press, Oxford, 1983)
25. C.W. Misner, K.S. Thorne, J.A. Wheeler, *Gravitation* (W. H. Freeman and Company, New York, 1973)
26. R.M. Wald, *General Relativity* (University of Chicago Press, Chicago, 1984)
27. J.M. Bardeen, W.H. Press, S.A. Teukolsky, Astrophys. J. **178**, 347 (1972). <https://doi.org/10.1086/151796>
28. R.P. Kerr, Phys. Rev. Lett. **11**, 237 (1963). <https://doi.org/10.1103/PhysRevLett.11.237>
29. C.M. Will, Living Rev. Relativ. **9**, 3 (2006). <https://doi.org/10.12942/lrr-2006-3>
30. B. Berche, S. Fumeron, F. Moraes, Phys. Rev. D **105**, 105026 (2022). <https://doi.org/10.1103/PhysRevD.105.105026>. arXiv:2205.05295 [gr-qc]
31. M. Milgrom, Astrophys. J. **270**, 365 (1983). <https://doi.org/10.1086/161130>
32. T. Harko, F.S.N. Lobo, S. Nojiri, S.D. Odintsov, Phys. Rev. D **84**, 024020 (2011). <https://doi.org/10.1103/PhysRevD.84.024020>
33. J. Binney, S. Tremaine, *Galactic Dynamics* (Princeton University Press, Princeton, 2008). <https://doi.org/10.1515/9781400828722>
34. R.C. Pantig, A. Övgün (2025). arXiv:2503.18585 [gr-qc]
35. E. Sucu, I. Sakalli, Phys. Rev. D **111**, 064049 (2025). <https://doi.org/10.1103/PhysRevD.111.064049>
36. Z. Stuchlík, M. Kološ, Mon. Not. R. Astron. Soc. **451**, 2575 (2015). <https://doi.org/10.1093/mnras/stv1120>. arXiv:1603.07339 [astro-ph.HE]
37. G. Török, Astron. Astrophys. **440**, 1 (2005). <https://doi.org/10.1051/0004-6361:20042558>. arXiv:astro-ph/0412500 [astro-ph]
38. R. Fiorito, L. Titarchuk, Astrophys. J. **614**, L113 (2004). <https://doi.org/10.1086/425736>. arXiv:astro-ph/0409416 [astro-ph]
39. D. Foreman-Mackey, D.W. Hogg, D. Lang, J. Goodman, Publ. Astron. Soc. Pac. **125**, 306 (2013). <https://doi.org/10.1086/670067>. arXiv:1202.3665 [astro-ph.IM]
40. A. Zhadyranova, M. Koussour, S. Bekkhozhayev, V. Zhumabekova, J. Rayimbaev, Phys. Dark Universe **45**, 101514 (2024). <https://doi.org/10.1016/j.dark.2024.101514>
41. F. Abdulkhamidov, P. Nedkova, J. Rayimbaev, J. Kunz, B. Ahmedov, Phys. Rev. D **109**, 104074 (2024). <https://doi.org/10.1103/PhysRevD.109.104074>
42. C. Liu, H. Xu, H. Siew, T. Zhu, Q. Wu, Y. Zhao, arXiv e-prints (2023). <https://doi.org/10.48550/arXiv.2305.12323>. arXiv:2305.12323 [gr-qc]
43. J. Rayimbaev, S. Murodov, A. Shermatov, A. Yusupov, Eur. Phys. J. C **84**, 1114 (2024). <https://doi.org/10.1140/epjc/s10052-024-13463-5>
44. G. Mustafa, E. Demir, F. Javed, S. Maurya, E. Güdekli, S. Murodov, F. Atamurotov, Phys. Dark Universe **46**, 101708 (2024). <https://doi.org/10.1016/j.dark.2024.101708>
45. A. Caliskan, G. Mustafa, T. Naseer, S.K. Maurya, E. Güdekli, S. Murodov, F. Atamurotov, J. High Energy Astrophys. **44**, 99 (2024). <https://doi.org/10.1016/j.jheap.2024.09.005>
46. B. Rahmatov, M. Zahid, J. Rayimbaev, R. Rahim, S. Murodov, Chin. J. Phys. **92**, 143 (2024). <https://doi.org/10.1016/j.cjph.2024.09.002>
47. S.E. Motta, T.M. Belloni, L. Stella, T. Muñoz-Darias, R. Fender, Mon. Not. R. Astron. Soc. **437**, 2554 (2014). <https://doi.org/10.1093/mnras/stt2068>. arXiv:1309.3652 [astro-ph.HE]
48. D.R. Pasham, T.E. Strohmayer, R.F. Mushotzky, Nature **513**, 74 (2014). <https://doi.org/10.1038/nature13710>